We thank the two reviewers for their insightful remarks. In response to these remarks, we have made a number of major changes in the manuscript. We first describe the major changes and then respond to individual comments. The revised manuscript and supplementary material are attached below.

Major Changes to the manuscript

1. In our original manuscript, we measured velocities from common offset GPR records by isolating diffractions through Plane Wave Destruction filtering, migrating the filtered data through a suite of constant velocities, and then computing the Varimax norm by isolating individual diffractions or groups of diffractions. This approach required defining the region of interest, viewing the migrated image that corresponded to the peak varimax value, and evaluating the quality of the velocity pick by inspecting the migrated image.

   In our revised manuscript, we compute the varimax norm in sliding windows that encompass the entire time section and have with a fixed width of ~10 meters. The result is a continuous set of velocity estimates along the GPR profile. Spurious picks are suppressed by smoothing the results in x. The revised method does not require inspection of the migrated images.

2. In our original manuscript, we presented two field data sets with independent snow density, depth, and SWE measurements. In the revised we include four additional field data sets with coincident manual observations. These data are included in our validation of the method, results from individual data sets as well as our manual snow density measurements are included in a supplementary materials file.

3. There was some confusion regarding our analysis of radar attenuation our dry snow assumption. Since the main focus of our paper is to estimate the radar velocity and thus the density of dry snow and the attenuation discussion detracts from this focus, we have reduced this discussion to one paragraph and moved it to *Section 2.7 Estimating SWE*.

4. We determined that the second synthetic data set, which was used to test the ability of the method to resolve lateral velocity changes, was redundant and we have removed it from the revised manuscript. Although the remaining synthetic data set has a constant snow velocity, the changing snow depths cause the migration velocity to vary along the profile (Figure 5, revised manuscript).

Response to reviewer comments:

Reviewer #1

(Reviewer Comments in italics)

General Comments:

In this paper, the authors attempt to apply established techniques from the exploration seismology literature to the problem of measuring Snow Water Equivalent (SWE) using constant offset GPR with the stated goal of simplifying that process while obtaining reliable results. The manuscript goes on to detail the application of these complicated methods to a few lines of field data with exceedingly limited success at producing results and processing flows that are neither reliable or simple. Given these results (as presented and described in the body of the manuscript itself) the concluding statements that "the processing flow that we presented in this paper proved to be an efficient way to measure radar velocities within seasonal snow" (Line 508) and "the method requires less processing time than visually scanning each migrated image and could make GPR a more attractive tool for estimating SWE at the watershed scale" (Line 509) are un- supported.

In response to your general, specific and technical comments, we have made a number of major changes in the manuscript.

1. Most significantly, we have eliminated the need for examining isolated diffractions in the GPR image. In the revised manuscript, we now compute the Varimax Norm in ~10-meter-wide sliding windows that span the entire time section. The result is a continuous set of varimax curves along the GPR profile and choosing the peak of each curve provides a

continuous estimate of the migration velocity along the profile. Although some of these curves provide spurious velocity estimates, smoothing the velocity picks in the horizontal direction reduces the influence of spurious velocity picks.

2. Our revised manuscript includes the results of six field GPR data sets, four pits, and 86 probed depth observations.

3. To qualitatively asses the efficiency of the method, we include an example of the processing time required for one 100 meter long GPR profile on a 2016 MacBook Pro with a 2 GHz processor. Lines (727-734):

> "One of our main goals was to produce a processing flow that allows for the rapid processing of common offset GPR data with minimal user interaction. The two most time computationally expensive parts of the processes are the migrations and the varimax calculations. As an example, on a 2016 MacBook Pro with a 2GHz processor, for the ~ 100-meter-long Line 4, performing 51 migrations takes approximately 5 minutes, the varimax calculation takes about half as long, and the PWD filtering takes a few seconds. The most time-consuming part of the process is picking the arrival times of snow surface and ground surface reflections."

Specific Comments:

The paper states that the "primary purpose of this study is to simplify the process of measuring GPR velocity in seasonal snow and obtain reliable SWE estimates" (Line 444) yet it accomplishes neither:

We admit that the word "simplify" was the wrong word to use. The goal of our study is to develop an efficient method for obtaining GPR velocities in seasonal, and thus snow densities, from common-offset GPR data. Additionally, we sought to minimize the amount of human interpretation throughout the process.In the revised manuscript, this sentence reads (lines 664-666):

"The primary purpose of this study is to develop an efficient processing flow for measuring GPR velocity and thus snow density SWE from common-offset data that requires a minimum amount of human interpretation."

Comparisons between our GPR derived estimates of depth, density, and SWE are summarized in Table 2 and in lines 434 to 442 of the revised manuscript. Aside from Line 3, which was located 1.5 meters off of Pit 2 and measured a shallower snowpack than observed in the pit, our GPR derived density and SWE estimates agree with manual measurements within 13% for density and 8% for SWE.

In terms of processes, simplification, the adaptation of Fomel's seismic approach (Line 133) and the NSE metric (Line 477) are gratuitously complicated, fail due to data quality issues (Line 230), and are not justified given the limited data set. There is no case made that the claims of efficiency (e.g. Line 221, Line 508) address actual measurement and processing bottlenecks or are even accurate. Further, once implemented these techniques still require frequent and substantial manual interventions (Lines 230, 377, 447, 460, and 462) culminating in the authors' suggestion that wavelength scale "point diffractors suitable for this type of analysis can be scouted for ahead of time during summer months or on aerial photographs" (Lines 499). Traditional GPR methods are much simpler than this (e.g. do not require advance scouting or aerial observation).

The results presented in our revised manuscript include six field data sets, 4 snow density pits, and 86 probed depth measurements. Utilizing our revised processing flow, we get similar results to those presented in the original manuscript, but with more data and without intervention.

Our results are summarize in Table 2 and in lines 700-708 of the revised manuscript:

"To validate the method, we compared estimated snow densities, depths, and SWE to observations made in four snow pits and to 86 probed snow depth measurements. The results are summarized in Table 2 and in Figure 9. If we exclude the two obvious outliers (Figure 10a), the RMS error for our depth predictions for the remaining 88 depth observations is 12% of the mean snowdepth observation. The RMS error for snow density and SWE relative to the mean observed values are 15% and 18%. Averaging the velocities across the entire line (Figure 10 red crosses) reduce the difference between predicted and observed depth values to an RMS error of 9%, suggesting that lateral variations in snow velocity are minimal. Averaging the velocities across the entire line reduces the RMS errors for density and SWE to 8% and 10%, respectively. "

We have removed the statement about scouting for point diffractors and instead comment on the high likelihood of encountering such objects in mountain watersheds (Lines 755-761):

"The data presented in this paper contained an abundance of diffractions located near the soil/ground interface allowing an average velocity for the entire snowpack to be obtained. These events are likely due to small-scale variations in surface topography, rocks, and/or vegetation along the ground surface, which may not be present in all environments. However, we note that mountain watersheds free of vegetation, small undulations in surface topography, and surface rocks are probably rare. Thus, the method may be useful in many regions where seasonal snowpacks exist."

In terms of reliable SWE estimation, the authors show that the presented approach "does not allow us to confidently differentiate between dry snow and moist snow" (Line 350). Further, authors show that the collected data does not exhibit the frequency dependent attenuation upon which the entire approach depend (Line 318 and Line 331) and even though "within uncertainty bounds there is no resolvable frequency change" (Line 440) the authors go on to use that uncertainty speculate that "there may be up to a 36 MHz shift" and then estimate a volumetric water content from it (Line 442) even though nothing suggests the existence of such a shift beyond the authors' assumption and assertion it should exist (Line 318). This is inappropriate and, as written, likely invalidates the results and conclusions of the paper. Further, the lack of observed frequency dependence is likely due to an actual lack of frequency dependence in radar attenuation in ice for frequencies below 1 GHz (Gudmandsen, 1971). This must be addressed. At the very least, the authors' statement "averaging mean snow-densities from manual observations may be a better strategy" (Line 489) makes it clear that the stated goal to "obtain reliable SWE estimates" (line 144) was not met.

We apologize for the confusion regarding radar attenuation in wet snow and its relationship to volumetric water content. We agree that in ice (or dry snow) the signal attenuation is negligible. It is the presence of water in the snowpack and the high contrast between the dielectric properties of dry snow and water that cause the attenuation of the GPR signal (see Bradford et al., 2009). Since the attenuation coefficient radar waves propagating in water is a linear function of frequency (Turner and Siggins, 1994), we expect to see a systematic decrease in higher frequency energy that is represented by a systematic decrease in the mean frequency content of the signal.

We recognize that our discussion of radar signal attenuation was a distraction from the main point of our paper and we have reduced the discussion of signal attenuation to one paragraph and moved it to **Section 2.7 Estimating SWE**. In addition, we have not used this analysis to report the maximum volumetric water content within our data resolution.

The revised discussion of radar attenuation (Lines 417-432) reads:

"In this paper, we are primarily concerned with measuring radar velocities and we assume that our data measure the properties of dry snow. The real part of the dielectric constant for water (~80) is much larger than that of snow (~1.5 - 2) and the imaginary part, which describes the attenuation of the signal, is non-negligible (Bradford at al., 2009). The dry snow assumption can be tested from the data by analyzing the attenuation properties of the snowpack (Bradford et al., 2009). The attenuation coefficient for radar waves in water is frequency-dependent (i.e. Turner and Siggins, 1994), with the higher frequencies attenuating more rapidly that the lower frequencies because they go through more cycles per distance traveled. When liquid water is present in the snow, the ground reflection will have a lower mean frequency content than a reference event (the snow reflection for the snowmobile collected data and the direct arrival for the skier-pulled data). To test the dry snow assumption, we calculate the maximum local instantaneous frequency (Fomel, 2007) within a time window surrounding the event of interest then average this value across all of the traces in the GPR image. The standard deviation provides an estimate of the measurement uncertainty. We note that at 500 MHz, a small shift in frequencies results in a non-negligible volumetric water content.."

Technical Corrections:

Line 107: Add an explanation and citation for "targets that have lateral dimensions that approximate the wavelength of the signal".

The diffraction literature makes reference to objects that are of similar dimension to the signal wavelength as well as to the first Fresnel zone. In consideration of our analysis depicted in Figure 1, we suggest that the Fresnel zone is more appropriate for our purposes. Lines 129-132 read:

"In this paper, we are specifically interested in targets that have lateral dimensions that are less than the Fresnel zone. These objects scatter energy in all directions and appear on the raw GPR image as hyperbolic events, called diffractions (Landa and Keydar, 1998).“

Citation:

Landa, E. and S. Keydar.: Seismic monitoring of diffraction images for detection of local heterogeneities, *Geophysics*, 63, 1998.

Lines 122: Why mention the 800 MHz data if it’s not used in the analysis? Consider removing.

We agree with this comment and the revised manuscript does not mention the 800 MHz data.

Line 202: This entire paragraph has a level of detail that seems inappropriate for a journal manuscript. Consider dropping or revising.

We think that this paragraph may be useful for readers who are unfamiliar with migration and have kept it in the revised manuscript.

Line 235: Provide a justification for the “equally likely” claim.

Thank you for this comment. We have justified our uncertainty estimate by comparing images migrated at different velocities to the corresponding varimax value. We found that images that were visually indistinguishable corresponded to varimax values that were greater than approximately 95% of the maximum. (See Figure 2 of the revised manuscript). Because the migrated images were indistinguishable to the human eye, we interpret these migration velocities to be valid velocity estimates and use them as upper and lower bounds on the true velocity.

Line 251: The units of the left and right side of this equation do not match.

Thank you for pointing out this error. The equation should be:

$$V_{snow} = \sqrt{\frac{V_{mig}^2 t_{soil} - V_{air}^2 t_{snow}}{t_{soil} - t_{snow}}}$$

and we have fixed this in the revised manuscript.

Line 318: Add an explanation and citation for "the coefficient increases with increased frequency" and address the fact that, in ice and below 1 GHz it does not (Gudmandsen, 1971).

We have added a citation and explanation. In the revised manuscript Lines 422-432 read:

"The attenuation coefficient for radar waves in water is frequency-dependent (i.e. Turner and Siggins, 1994), with the higher frequencies attenuating more rapidly that the lower frequencies because they go through more cycles per distance traveled. When liquid water is present in the snow, the ground reflection will have a lower mean frequency content than a reference event (the snow reflection for the snowmobile collected data and the direct arrival for the skier-pulled data). To test the dry snow assumption, we calculate the maximum local instantaneous frequency (Fomel, 2007) within a time window surrounding the event of interest then average this value across all of the traces in the GPR image. The standard deviation provides an estimate of the measurement uncertainty. We note that at 500 MHz, a small shift in frequencies results in a non-negligible volumetric water content."

Citation:

Turner, G., and A. F. Siggins.: Constant Q attenuation of subsurface radar pulses, *Geophysics*, 59, 1994.

Line 155, 404, and others: Justify uncertainties and provide basis throughout the manuscript for uncertainties that are currently just asserted.

Lines 341-343:

"We use the upper and lower bounds on our velocity estimates to compute upper and lower bounds on all subsequent calculations."

Lines 401-403

"To propagate our velocity uncertainty estimates through the dix equation, we assign a travel-time uncertainty of 0.2 ns to our travel-time observations and use Eq. 5 along with our velocity uncertainty estimates to compute upper and lower bounds on the snow velocity."

Reviewer # 2

The paper by St. Clair and Holbrook describes a novel approach for determining the snow-water-equivalent (SWE). I have read the well-written paper with great interest, and I judge it a useful contribution for the Cryosphere community. Before the paper can be accepted, I suggest that the authors address the following issues.

1. There are inconsistencies and errors with the units. I suggest that they should use mks units throughout the entire manuscript.

In the revised manuscript we use meters for units of distance (and depth) and SWE, m/ns for radar velocity and kg/m^3 for snow density.

2. It is often referred to Line 7 and Line 19. Without a map showing these profiles and/or a table describing the characteristics of the profiles, these references are not helpful. Since there seem to be only lines 7 and 19 discussed, it would make sense to rename them to line 1 and line 2.

We have provided tables to describe each field data set. Table 1 summarizes snowpits 1-4. Table 2 describes the GPR data and reports data of acquisition, the acquisition mode (ski or snowmobile), the type of independent observations we compared our results to, and the difference between GPR estimated values and manually measured values.

3. It is my understanding that the methodology works only for dry snow and that de- termining the liquid water content from the GPR data was not successful. These two facts should be stated more explicitly.

We have made this more explicit in several parts of the revised manuscript:

Lines 99-101:

"Since our primary goal is to develop a method for quick velocity estimations, we assume that the snow we are measuring is dry."

Lines 417-418;

"In this paper, we are primarily concerned with measuring radar velocities and we assume that our data measure the properties of dry snow."

4. Figures 10 and 11 indicate that the GPR estimated depths are systematically smaller compared with the probe depths. This should be discussed.

After reprocessing the data with the new approach, there is not a systematic error in the depth predictions.

5. Further discussion is required on the basic assumption of the approach that the scattering bodies can be considered as a point diffractor. I guess that the scattering occurs mostly at sizeable boulders. Therefore, I am not convinced that the point scatterer assumption is really justified. The diffraction hyperbola of a finite sized scattering body is expected to appear wider in a GPR profile, which would likely result in an over- estimation of the snow velocity. Consequently, one would thus rather overestimate the snow depth, but, as mentioned in point 4, the opposite seems to be the case.

Thank you for this comment. We have evaluated the effects of non-finite point diffractors, or diffracting objects that approach the dimension of the Fresnel zone. Figure 1 illustrates the effects of a lateral diffractor dimension and curvature on the peak value of the varimax norm. We also include the following discussion:

Lines 286-305:

"To assess possible errors in the migration velocity analysis, we applied our workflow to a synthetic data set generated from diffractors of varying size. The Fresnel radius is given by $R_f = \sqrt{\frac{z\lambda}{2}}$ (Sheriff, 1980) where z is depth and λ is the dominant wavelength. Figure 1 shows the effect of such an event on V. We created five synthetic diffractions with migration a migration velocity of 0.24 m/ns. The first four (Figure 1a) correspond to rectangular objects at 1 meter depth with horizontal dimensions 0.1, 0.2, 0.3 and 0.4 meters, and thickness of 0.03 m and the fifth corresponds to a circular object with a radius of 0.4 meters (close to R_f for the 500 MHz ricker wavelet used to generate the diffractions). The corresponding varimax curves for the windows shown in Figure 1a are plotted in Figure 1b. The V curves are peaked at 0.24 m/ns for all of the rectangular diffractors, with flatter (less well-resolved) peaks as the horizontal dimension of the diffracting object increases, suggesting a larger uncertainty in the velocity estimate. The peak V value for the circular diffractor is at 0.268 m/ns, indicating that curved objects with lateral dimensions close to the size of the Fresnel zone may continue to focus at velocities higher than their true velocity. Finally, Figure 1c shows the V curve for the entire image, peaked at the correct velocity of 0.24 m/ns. This analysis suggests that the peak V value will correspond to the correct velocity if the majority of the diffractions correspond to objects much than R_f..”

Lines 709-726:
“The greatest potential for systematic error in this analysis is the presence diffracting objects whose dimensions exceed the radius of the first Fresnel zone. The field data offer the opportunity to evaluate the influence of diffractor size on velocity estimates. Line 1, for example, shows four prominent diffractions between 50 and 70 meters. The Varimax norm has a maximum value at 0.256 m/ns, which is the velocity that focuses the two leftmost diffractions (Figure 6c). The diffractions on the right are clearly not focused because they are caused by an object (most likely a log) with a radius greater than the first Fresnel zone. Because the leftmost two have a higher amplitude then the others, they have the largest influence on the varimax value. Thus, although there are clearly events in the field data that have the potential to give erroneous results, our results suggest that reliable velocity estimates can be achieved so long as the majority of the diffracted energy is related to objects that can be considered point diffractors.
.”

6. Some of the figures are lacking proper axis labeling.

In our original manuscript many of the plots did not have axes labels, if the plots immediately above or adjacent to them had the same axis. The lower and leftmost plots had the axes labels on them. In the revised manuscript, all plots have axes labels.

7. It seems that in Figures 7 and 9 only portions of the GPR profiles are shown. This should be clarified.

In the revised manuscript, all figures depicting data show the entire data set.

Measuring snow water equivalent from common offset GPR records through migration velocity analysis

James St. Clair[1,2] and W. Steven Holbrook[1,3]

[1]Department of Geology and Geophysics, University of Wyoming, Laramie, WY, 82071, USA.

[2]Department of Geological Sciences, University of Idaho, Idaho Falls, ID, 83402, USA.

[3]Dept. of Geosciences, Virginia Tech, Blacksburg, VA 24061

Deleted: [1]University of Wyoming, Department

Deleted: [2]University of Idaho, Department

Deleted: ... [1]

Formatted: Font:Not Italic

Formatted: None

Abstract

Many mountainous regions depend on seasonal snowfall for their water resources. Current methods of predicting the availability of water resources rely on long-term relationships between stream discharge and snow pack monitoring at isolated locations, which are less reliable during abnormal snow years. Ground-penetrating-radar (GPR) has been shown to be an effective tool for measuring snow water equivalent (SWE) because of the close relationship between snow density and radar velocity. However, the standard methods of measuring radar velocity can be time consuming. Here we apply a migration focusing method originally developed for extracting velocity information from diffracted energy observed in zero-offset seismic sections to the problem of estimating radar velocities in seasonal snow from common-offset GPR data. Diffractions are isolated by plane-wave-destruction filtering and the optimal migration velocity is chosen based on the varimax norm of the migrated image. We then use the radar velocity to estimate snow density, depth, and SWE. The GPR-derived SWE estimates are within 6% of manual SWE measurements when the GPR antenna is coupled to the snow surface and 3-21% of the manual measurements when the antenna is mounted on the front of a snowmobile ~0.5 meters above the snow surface.

Formatted: Font:Italic

Deleted: the

Deleted: relationship

Deleted:

Deleted: 3

Deleted: 18

1. Introduction

Many regions of the world are critically dependent on seasonal snowfall for their water resources; accurate estimates of how much water is stored in mountain landscapes are necessary to manage this resource. In the United States, a large network of SNOTEL sites provide continuous information about snow depth, density, and snow water equivalent that are used to make water availability predictions (Serreze et. al., 1999). While these sites provide valuable information at a site, scaling these point measurements up for basin or grid scale estimates can be challenging (Molotch and Bales, 2005). Currently, these data are used to develop empirical relationships between SWE and nearby stream discharge. These predictions are most accurate during average years and may be not reliable during abnormal years (Bales et al., 2006), thus there is a need to develop new and reliable methods for estimating SWE at a basin scale.

Several previous studies have demonstrated that Ground-Penetrating-Radar (GPR) can be used to measure SWE (e.g. Bradford et al., 2009, Tiuri et al., 1984, Holbrook et al. 2016). Tiuri et al. (1984) showed that at microwave frequencies, the real part of the dielectric constant for dry snow, which governs the velocity, is almost completely determined by the bulk density of snow. However, when liquid water is present, both the real and imaginary parts are needed to determine the volumetric water content of the snow. The complex dielectric constant can be measured by analyzing both the velocity and attenuation characteristics of the snow (Bradford at al., 2009). In the simplest case of dry snow, bulk density can be estimated directly from radar velocity. Snow depth can be measured from the two-way travel time of the radar

Deleted: and

Deleted: the mountains

Deleted: there is currently

Deleted: , where automated sensors

Deleted: the

pulse between the snow surface and the ground surface and the velocity. SWE can then be calculated as the product of snow density and snow height.

Velocity measurements can be made from the surface in several ways. Common-midpoint gathers (CMP), where the distance between transmitting and receiving antennas is steadily increased about a central location, provide highly accurate measurements; the two-way travel-time to subsurface reflectors is a function of offset and velocity. Collecting CMP's requires separable antennas, and it can be time-consuming to both collect and process these data. Common-offset antennas, where both the transmitting and receiving antennas are housed in the same unit at a fixed offset, allow large amounts of data to be collected with minimal effort. Measuring the velocity from common offset data can be achieved through calibration from measured snow depths, modeling diffraction hyperbolae travel-times, or migration focusing analysis.

In this paper, we apply the migration velocity analysis (MVA) presented by Fomel (2007) to the problem of estimating radar velocities, and thus snow density and SWE, from 500 MHz common-offset GPR images. After testing the method on a synthetic data set, we estimate SWE from six field data sets. The first two data sets were collected by pulling the GPR along the snow surface, and the remaining four were collected with the GPR antenna mounted on the front of a snowmobile. To validate the method, we compare snow depth, density and SWE estimates to measurements made in pits and probed depth observations along the profiles. Since our primary goal is to develop a method for quick velocity estimations, we assume that the snow we are measuring is dry. The GPR-derived estimates agree with manual SWE measurements within the estimated uncertainties.

Deleted: increases as

Deleted:

Deleted: done in several ways including

Deleted: and

Deleted: focusing analysis, or migration

Deleted:

Deleted: two

Deleted: sets

Deleted: then

Deleted: two

Deleted: set was

Deleted: second data set was

Deleted: Compared to manual

Deleted: measurements, the

Deleted:

Deleted: with

2. Methods

GPR surveys utilize high-frequency, broadband electromagnetic signals. The signal is generated at the transmitting antenna and propagates in three dimensions at velocity given by $v = c/\sqrt{\kappa'}$, where c is the speed of light in a vacuum and κ' is the real part of the dielectric constant. Signal attenuation is frequency-dependent and can be approximated as $\alpha \approx \sqrt{\frac{\mu_0}{\kappa'}\frac{\kappa''}{2}}\,\omega$, where μ_0 is the magnetic permeability of free space and κ'' is the imaginary component of the dielectric constant (Bradford, 2007). While both κ' and κ'' are frequency dependent, within the typical frequency range utilized for GPR studies, only κ'' exhibits strong variations with frequency; in dry snow $\kappa'' \approx 0$ (Bradford et al., 2009).

When a GPR signal encounters a boundary between subsurface materials with contrasting dielectric constants, some of the energy is reflected back and recorded by a receiving antenna. In this paper, we are specifically interested in targets that have lateral dimensions that are less than the Fresnel zone. These objects scatter energy in all directions and appear on the raw GPR image as hyperbolic events, called diffractions (Landa and Keydar, 1998), whose shape depends on the depth of the object and the velocity of the overlying media (i.e. Claerbout, 1985). The velocity information contained in diffractions can be extracted by fitting hyperbolic curves to the data or by migrating the image until the hyperbola is collapsed to a point or "focus." The latter process is called migration velocity analysis (MVA). In this paper, we follow an approach described by Fomel (2007) and develop a semi-automated MVA program in Matlab for the purpose of measuring radar velocities in seasonal snow. The processing flow consists of three steps: 1. Separate diffractions from reflections through

Deleted:

Deleted:

Deleted: approximates

Deleted: Both

Deleted: however

Deleted: the

Deleted: approximate

Deleted: wavelength of the signal.

Deleted: ,

Deleted: .

Deleted: 2002

Plane-Wave-Destruction (PWD), 2. Migrate the filtered images at a range of potential velocities, and 3. Use the varimax norm as a measure of diffraction focusing to pick velocities.

2.1 Data Acquisition

2.1.1 GPR data

During February and March 2015, we collected GPR, snow density, and snow-depth data in the Medicine Bow Mountains, SE Wyoming. The GPR data were acquired with a Mala pulse radar system with a center frequencies of 500 MHz. The data were collected in two ways. In one configuration (Lines 1 and 2), we mounted the GPR antenna in a plastic sled and pulled it behind a skier. The unit was set to fire continuously at a rate of 20 traces per second and the sample interval on each trace was 0.3223 ns. In the other configuration (Lines 3, 4, 5 and 6) the antennas were mounted on an aluminum frame attached to the front of a Polaris RMK 600 snowmobile. The unit was set to fire at a rate of 100 traces per second and the sample interval was 0.3181 ns. Mounting the GPR antenna in front of the snowmobile allows us to measure undisturbed snow as well as providing a snow-surface reflection, which can be used to analyze the attenuation properties of the snow (Bradford et al., 2009). In both cases, we kept track of our position with a Trimble R8 GPS unit that recorded our location at 1-second intervals.

2.1.2 Snow depth and density data

To validate our snow density and velocity estimates from the GPR data, we manually measured snow depth and densities (Table 1). On Lines 1, 2, 3 and 4 we dug snow pits and located them with a handheld Trimble GPS unit. To measure snow densities, we used a 0.001

Deleted: the process of

Deleted: Acquistion

Deleted: using two common offset antennas

Deleted: and 800

Deleted: In this paper, we only present 500 MHz data because the lower frequencies show higher amplitude and more continuous ground reflections and produces better results when separating reflections from diffractions. ... [2]

Deleted: GPR

Deleted: Line 19

Deleted: in time

Deleted: Line 7

Deleted: .

Deleted: Line 7, we used a probe to measure snow depths at 5-meter intervals along the profile

Deleted: two

Deleted: ; pit

Deleted: probe sites were

Deleted: with a measuring tape. On Line 19, we dug one snow pit and located it cubic meter, wedge-shaped snow sampler and a scale that is accurate within 5-10 grams. We made snow density measurements at 10 cm intervals in the sidewall of the snow-pits starting from the snow surface and continuing to the ground. Pit locations were chosen based on the presence of diffractions near the snow/ground interface after viewing the GPR images in the field. On lines 4, 5, and 6 we measured snow depth at regular intervals with a probe.

Deleted:

Probed depth measurements are subject to uncertainties due to uneven ground and deviations in probe angle. We estimate our depth measurements to be accurate within +/- 5 cm. Snow density observations are subject to over and under sampling and we assign an uncertainty of +/- 5 g/cm^3. We calculate the average density for each pit profile assigning each snow density observation to a 10 (+/-1) cm column of snow and performing a weighted sum. Propagating the uncertainties through the averaging process yields uncertainty estimates of 10-14 % of the averaged value, consistent with uncertainty estimates for snow pit density measurements reported by Conger and McClung (2009).

2.2 Pre-Processing the GPR data

Prior to MVA we use MATGPR R3 (Tzanis, 2010) to apply several basic processing steps to the GPR data including: 1. Reset trace to time-zero, 2. Trim time window, 3. Interpolate traces to equal spacing using the GPS data, 4. Bandpass filter from 100 to 1000 MHz, 5. median filter to remove antenna ringing, and 6. Scale the amplitudes by t^2.

Deleted: and

Deleted: .

2.3 Plane-Wave-Destruction

Plane wave destruction (PWD) is a predictive filtering method designed to suppress events in a seismic or GPR record having a particular dip (Claerbout, 1992; Fomel, 2002). The GPR image is modeled as the local superposition of plane waves described by the differential equation (Fomel, 2002):

$$\frac{dP}{dX} - \sigma \frac{dP}{dt} = 0 \qquad (1)$$

where $P(x,t)$ is the wave-field and $\sigma(x,t)$ is the local dip. Equation 1 provides the means for predicting a trace in the GPR image from its neighbor as a function of local dip. Fomel's (2002) three-point filter is derived from this equation:

$$C(\sigma) = \begin{array}{cc} \frac{(1+\sigma)(2+\sigma)}{12} & -\frac{(1-\sigma)(2-\sigma)}{12} \\ \frac{(2+\sigma)(2-\sigma)}{6} & -\frac{(2+\sigma)(2-\sigma)}{6} \\ \frac{(1-\sigma)(2-\sigma)}{12} & -\frac{(1+\sigma)(2+\sigma)}{12} \end{array} \qquad (2)$$

where σ is the local dip and the filtering is accomplished by convolving (2) with the GPR image. The goal is to suppress continuous reflections that have small dips (such as snow layering and the ground surface) compared to the steeply dipping diffraction limbs.

To estimate local dips, we make an initial guess σ_0 for the dip and solve the set of equations

Deleted: ,

Deleted: solves

Deleted: ,

Deleted: Since we do not know the local dips, we use the stencil in equation 2 to estimate them directly from the data.

Deleted: (usually zero)

$$\begin{pmatrix} \boldsymbol{C}'(\sigma_0)\boldsymbol{d} \\ \varepsilon\boldsymbol{D} \end{pmatrix} \Delta\sigma = \begin{pmatrix} -\boldsymbol{C}(\sigma_0)\boldsymbol{d} \\ 0 \end{pmatrix} \tag{3}$$

for $\Delta\sigma$. Here, $\boldsymbol{C}(\sigma)$ denotes the convolution of the filter with the data ($\boldsymbol{d}$), $\boldsymbol{C}'(\sigma)$ is the derivative of the filter with respect to σ ($\boldsymbol{C}'(\sigma)\boldsymbol{d}$ is a diagonal matrix), **D** is the gradient operator, and ε is a weighting parameter that controls the smoothness of the estimated dip field. Imposing smoothness constraints on the dip field estimate ensures stability in the solution and helps target the reflections in the image, since they generally show higher amplitudes and are more laterally continuous than the diffractions we seek to preserve. The estimated dip field is then used to filter the data.

2.4 Migration

Migration is the process that moves reflected and diffracted energy in a seismic or GPR record to its true location in the subsurface (i.e. Claerbout, 1985). The quality of the migration process depends on the accuracy of the velocity estimate. When the correct migration velocity is chosen, diffraction hyperbolas will collapse to a compact "focus." With too low a velocity, the hyperbola will only be partially collapsed, while a velocity that is too high will cause the hyperbola to be mapped into a "smile".

For the MVA analysis, we migrate the entire image through a suite of velocities (0.19 to 0.29 m/ns in increments of 0.002 m/ns) using MATGPR's implementation of the Stolt algorithm (Stolt, 1955). The Stolt algorithm performs the migration in the frequency wave-number domain and is computationally efficient. To reduce computational time, we modified the code to perform all the migrations in one function call so that the forward Fourier transform is only performed once.

Deleted: .

Deleted: Too

Deleted: of

Deleted: and

Deleted: ."

Formatted: Indent: First line: 0.5"

Deleted: initial

2.5 Velocity Picking

After PWD filtering and migrating the data through the suite of velocities, the next task is to use a focusing indicator to pick the image that is optimally focused. Following Fomel (2007), we use the varimax norm (V):

$$V = \frac{N\sum_{i=1}^{N} s_i^4}{\left(\sum_{i=1}^{N} s_i^2\right)^2} \quad (4)$$

where s_i is the amplitude of the *i*th sample and N is the number of samples included in the calculation. V is a measure of the "simplicity" of a signal (Wiggins, 1978). Since the simplest possible signal is a spike and the optimal migration velocity will map hyperbolas to the most compact "focus", the maximum V value will correspond to the image migrated with the optimal velocity.

To assess possible errors in the migration velocity analysis, we applied our workflow to a synthetic data set generated from diffractors of varying size. The Fresnel radius is given by $R_f = \sqrt{\frac{z\lambda}{2}}$ (Sheriff, 1980) where z is depth and λ is the dominant wavelength. Figure 1 shows the effect of such an event on V. We created five synthetic diffractions with migration a migration velocity of 0.24 m/ns. The first four (Figure 1a) correspond to rectangular objects at 1 meter depth with horizontal dimensions 0.1, 0.2, 0.3 and 0.4 meters, and thickness of 0.03 m and the fifth corresponds to a circular object with a radius of 0.4 meters (close to R_f for the 500 MHz ricker wavelet used to generate the diffractions). The corresponding varimax curves for the

Deleted: ,

Deleted: ... [3]

windows shown in Figure 1a are plotted in Figure 1b. The V curves are peaked at 0.24 m/ns for all of the rectangular diffractors, with flatter (less well-resolved) peaks as the horizontal dimension of the diffracting object increases, suggesting a larger uncertainty in the velocity estimate. The peak V value for the circular diffractor is at 0.268 m/ns, indicating that curved objects with lateral dimensions close to the size of the Fresnel zone may continue to focus at velocities higher than their true velocity. Finally, Figure 1c shows the V curve for the entire image, peaked at the correct velocity of 0.24 m/ns. This analysis suggests that the peak V value will correspond to the correct velocity if the majority of the diffractions correspond to objects much than R_f.

We choose to compute V in sliding windows that span the entire time section and have a user-defined width. Computing V in this way allows us to incorporate many diffraction events and maximize the likelihood that the bulk of the diffractions satisfy the point diffractor assumption. Moreover, sliding windows offer the potential to capture lateral variability in snow density.

After computing V for the entire data set, we choose the maximum V value in each window to get an estimate of the migration velocity. Noise in the filtered image, large diffracting objects, or a lack of diffractions may cause the peak of the Vnorm to correspond to an incorrect velocity. To reduce the influence of erroneous velocity picks, we smooth the picks in the lateral direction with a boxcar averaging filter the same width as the sliding window.

We use the shape of the upper portion of the V curve to estimate uncertainties in the velocity pick. Comparing the Vnorm curves for synthetic diffractions as well as those from our data, we find that Vnorm values that are greater than 95% of the peak value correspond to

Deleted: within

Deleted:

Deleted: windows, so that we can be sure to select

Deleted: hyperbolas that are well preserved after PWD filtering.

Formatted: Indent: First line: 0.5"

Deleted: choosing a

Deleted: , we compute V within this window for each

Deleted: migrated image panels and plot V against

Deleted: Due to noise

Deleted: and poorly preserved

Deleted: ,

Deleted: V plot may display multiple peaks. Plotting

Deleted: migrated images that

Deleted: peaks

Deleted: V plot allow us to verify that the diffractions are focused.

Deleted: After choosing a velocity, we

Deleted: We assume

Deleted: all velocities with V

Deleted: could be equally likely, which yields an migrated images that are indistinguishable to the human eye (Figure 2). We therefore obtain upper and lower bounds on our velocity estimate by finding the minimum and maximum velocities with Vnorm values equal to 95% of the maximum. We use the upper and lower bounds on our velocity estimates to compute upper and lower bounds on all subsequent calculations.

Deleted: bound on the velocity estimate that depend

Deleted: the sharpness of the V peak. This procedure yields uncertainty estimates of +/- 0.005-0.01 m/ns, which is comparable to the 0.005 m/ns reported in studies that rely on picking

Deleted: by visually comparing the migrated images (Bradford and Harper, 2005).

2.6 Dix Equation

The migration velocity is the RMS velocity of all of the material between the GPR antenna and the diffractor. When the GPR antenna is in contact with the snow and the diffractor is located at the base of the snow, we interpret the migration velocity to be the average velocity of the snow across the width of the diffraction hyperbola. When the GPR unit is mounted on the front of the snowmobile, the signal must pass through the air between the antenna and the snow-surface so that the migration velocity is higher than that of the snow. To find the snow-velocity from these data, we use the Dix equation (Dix, 1955):

$$V_{snow} = \sqrt{\frac{V_{mig}^2 t_{soil} - V_{air}^2 t_{snow}}{t_{soil} - t_{snow}}} \quad (5)$$

Deleted: $\sqrt{\left(\frac{V_{mig}^2 t_{soil} - V_{air}^2 t_{snow}}{t_{soil} - t_{snow}}\right)},$

where velocity subscripts refer to the migration velocity, the velocity in air, and the velocity within the snowpack and time subscripts refer to the two-way travel-times of the snow surface and soil surface reflections.

The Dix equation contains two important assumptions. First, the velocity of the snow must be approximately constant over the width of the hyperbola and second, the half-width of the hyperbola should be small compared to the depth of the diffractor (x << z). The diffractions in our data sets are approximately 4 to 5 meters wide; thus we assume that any lateral variations in snow density occur on a larger scale than this. If the second assumption is not valid, then the Dix velocity will be higher than the true velocity, resulting in a density estimate that is too low. The snow depths in our data range from ~1-2 meters, which is comparable to the half-width of the hyperbolas.

To determine the minimum snow depth that satisfies the x << z assumption, we traced rays from point diffractors at depths ranging from 0 to 5 meters through a 0.23 m/ns snowpack, representing a snow density of 0.358 g/cm^3 (see section 2.7), with a 0.5 meter thick air layer between the snow surface and the receiver positions (Figure 3). For each resulting travel-time curve, we obtained nine different estimates of the migration velocity by performing a least-squares fit to the travel-time data and successively reducing the widths of the hyperbolas from 10 to 2 meters in 1 meter increments. Using the Dix equation, we obtained estimates of the snow velocity as a function of diffractor depth and hyperbola width (Figure 4). The velocity estimates made with the Dix equation approach the true velocity as the diffractor depth increases and the hyperbola width decreases. For hyperbolas that are 4 to 5 meters wide (the average width that we observe in our data), the Dix velocity is within 2 percent of the true velocity when the diffractors are about 1.5 meters deep, 5 percent when the diffractors are about 1 meter deep, and 10 percent or greater when the diffractors are 0.5 meters deep. We conclude that the use of the Dix is justified for diffractors buried deeper than 1.5 meters beneath the snow surface.

Deleted:

Deleted: ,

Deleted: 1

Deleted: 2

Although the results of this analysis are only valid for travel-time modeling, the x << z assumption may be less severe for migration focusing analysis (see section 3.1). Diffraction amplitudes decrease with increasing horizontal distance from the diffractor location, thus the traces closest to the diffractor have the greatest contribution to the final image, suggesting that the Dix equation may give adequate results for diffractors that are less than 1.5 meters deep when velocities are estimated from MVA (we test this with our synthetic data set in section 3.1).

Deleted: first

To propagate our velocity uncertainty estimates through the Dix equation, we assign a travel-time uncertainty of 0.2 ns to our travel-time observations and use Eq. 5 along with our velocity uncertainty estimates to compute upper and lower bounds on the snow velocity.

2.7 Estimating SWE

To estimate SWE from the radar data, we need to know the depth of the snow and the snow density ($SWE = z_{snow}\rho_{snow}$). The depth can be found by picking the two-way travel-time of the ground reflection and, if applicable, the snow-surface reflection and then using the velocity estimate to convert time to depth. Using Eq. 1, we convert radar velocity to dielectric constant ($v = c/\sqrt{\kappa'}$) and estimate the density of dry snow with the empirical relationship (Tiuri et al., 1984):

$$\kappa'_d = 1 + 1.7\rho + 0.7\rho^2, \tag{6}$$

where κ'_d is the dielectric constant and ρ is the density of dry snow.

In this paper, we are primarily concerned with measuring radar velocities and we assume that our data measure the properties of dry snow. The real part of the dielectric constant for water (~80) is much larger than that of snow (~1.5 - 2) and the imaginary part, which describes the attenuation of the signal, is non-negligible (Bradford at al., 2009). The dry snow assumption can be tested from the data by analyzing the attenuation properties of the snowpack (Bradford et al., 2009). The attenuation coefficient for radar waves in water is frequency-dependent (i.e. Turner and Siggins, 1994), with the higher frequencies attenuating more rapidly that the lower frequencies because they go through more cycles per distance traveled. When liquid water is present in the snow, the ground reflection will have a lower mean frequency content than a reference event (the snow reflection for the snowmobile collected data and the direct arrival for the skier-pulled data). To test the dry snow assumption, we calculate the maximum local instantaneous frequency (Fomel, 2007) within a time window surrounding the event of interest then average this value across all of the traces in the GPR image. The standard deviation provides an estimate of the measurement uncertainty. We note that at 500 MHz, a small shift in frequencies results in a non-negligible volumetric water content.

3. Data and Results

Snow depth, density and SWE estimates for all of our GPR profiles and pits are summarized in Tables 1 and 2. Here we discuss the processing and describe results for a synthetic data set and two representative field data sets.

Formatted: Font:Bold

Deleted: however when liquid water is present in the snowpack the signal attenuates and the imaginary component

Deleted: can no longer be ignored. Tiuri et al. (1984) gave the following equation to relate the imaginary dielectric constant of snow to snow wetness at 1 GHz: ... [4]

Formatted: Not Raised by / Lowered by

Deleted: characteristics

Formatted: Not Raised by / Lowered by

Deleted: GPR data

Formatted: Not Raised by / Lowered by

Deleted: et

Formatted: Not Raised by / Lowered by

Deleted: .

Formatted: Not Raised by / Lowered by

Deleted:) and κ''_w can be computed with the Debye relaxation model. ... [5]

Deleted: we must estimate

Deleted: snow. Since the

Deleted: increases with increasing

Deleted: ,

Deleted: attenuate

Deleted: than

Deleted: . Thus, if there is

Deleted: it

Deleted: be manifested as

Deleted: reduced

Deleted: of the base of snow reflection with respect

Deleted: that bounds

Deleted: upper surface of

Deleted: snow. ... [6]

Deleted: frequency content of

Deleted: different events in

Deleted: GPR image

Deleted: compute the local instantaneous frequency attribute (Fomel, 2007). The local instantaneous frequency is computed in the same way as the instantaneous frequency except that smoothness constraints are imposed so that the calculations are less sensitive to noise in the data. We

Deleted: ... [7]

Deleted: changes in frequency result in non-negligi ... [8]

Formatted: Font:Not Bold

3.1 Synthetic test

As a first test on the reliability of migration focusing analysis for reconstructing radar velocities, we performed the analysis on a synthetic data set generated with REFLEX software. The synthetic data set was generated using a 500 MHz Kuepper wavelet sampled at 0.0332 ns and traces are 0.01 meters apart.

The synthetic model is 50 meters long and consists of a 0.5 meter thick layer of air overlying a 0.24 m/ns layer of snow (corresponding to a density of 0.29 g/cc) with depths that range from 0.5 to 5.7 meters. Beneath the snow is a 0.10 m/ns layer representative of soil. Along the snow/soil interface there are 16 diffractors buried at depths ranging from 0.5 to 5.7 meters. The purpose of this data set (Figure 5a) was to test the performance of the Dix equation on velocities estimated from the MVA analysis and, since the migration velocity changes as a function of snow depth, to see if we can resolve lateral variations in velocity.

After applying the PWD filter, the ground reflection was adequately suppressed (Figure 5b). We migrated the filtered image at 0.002 m/ns intervals from 0.18 to 0.28 m/n and measure the optimal migration velocity for each diffractor by computing V in an 8-meter-wide sliding window (Figure 5c). We use the Dix equation to convert the migration velocities to the velocity of the snow layer (Figure 5d). The average of all snow velocity measurements is 0.241 m/ns with a standard deviation of 0.002 m/ns.

There is no systematic relationship between the velocities recovered and the depth of the diffractor (Figure 5d). The shallowest diffractor was at ~0.5 m depth and the recovered velocity was 0.232 m/ns. The greatest differences between recovered and true velocities were for diffractors at depths of 0.5, 1.5, and 2.2 and 2.3 meters. Here the recovered velocities were

Deleted: two
Deleted: sets
Deleted: sets were
Deleted: 1
Deleted: first
Deleted: layer of snow
Deleted: 4a
Deleted: 4b
Deleted: 4c) within small windows centered over the apex of the hyperbola (Figure 4b).
Deleted: .
Deleted: 04
Deleted: 5
Deleted: 237
Deleted: 03, 1.54
Deleted: 1

0.232, 0.247 0.247, and 0.247 m/ns. The shallowest observation underestimates the true velocity, which is the opposite of the effect predicted by our travel-time modeling (Section 2.6, Figure 4). The observations for diffractors between 1.5 and 2.3 meters all overestimate the true velocity by approximately the same amount. We conclude that the Dix equation is appropriate for snowdepths of 0.5 meters and greater.

Although the snow in this synthetic model has a constant velocity, the migration velocity changes as a function of the snow depth due to the changing proportions of air and snow in the total travel path. Where the snow is shallow, the velocities are highest and where the snow is deep, the velocities are low. That the method is capable of resolving lateral velocity variations in this synthetic example is evident in Figure 5c, where the picked velocities are negatively correlated with snowdepth.

3.2 Ski-pulled GPR data

We collected two GPR profiles in the skier -pulled configuration on February 25, 2015, in below-freezing conditions. A representative line, Line 1 (Figure 6) is 74 meters long and shows an abundance of diffractions along the snow/ground interface, likely a result of small boulders, and a few isolated diffractions within the snowpack, most likely small trees, bushes or logs. After interpolation to equal spacing, trace spacing was 0.362 m. Since the antenna was coupled to the snow, we compare the average frequency of the direct wave to that of the soil reflection to determine whether there is any liquid water present in the snowpack. The average frequency of the direct arrival for every trace in the image along Line 1 is 410 MHz with a standard deviation of 10 MHz and the average frequency of the soil reflection across the whole

Deleted: 245, 0.246, and

Deleted: 245

Deleted: Notably,

Deleted: peak V value

Deleted: the diffractor located at 1.54

Deleted: depth corresponded to an image

Deleted: was clearly over-migrated and we would have rejected this measurement

Deleted: a real data set.

Deleted: The second model is 10 meters long with a snow layer that ranges from 1.9 to 2.7 meters thick with a velocity that increases from 0.257 m/ns at x=0, to 0.262 m/ns at x = 10 meters. There are seven diffractors along the soil/snow interface. The primary purpose of this data set (Figure 6a) was to see whether this method could resolve a lateral change in velocity. ... [9]

Deleted: Line 19 is a 74 meter long, skier pulled data set

Deleted: The data show

Deleted: or bushes (Figure 7a).

line is 457 MHz with a standard deviation of 42 MHz. The soil reflection appears to have a higher frequency content than the reference frequency, perhaps due to thin-layer "tuning" effects. Since we do not observe a decrease in frequency with travel time, we infer that there was no liquid water present in the snow on this day.

After the PWD filtering step we are left with many diffractions along the ground surface and a few isolated events within the snowpack (Figure 6b). We compute V in 10-meter-wide sliding windows and pick the velocity that corresponds to the peak value of V (Figure 5d, blue line). After smoothing these picks (Figure 6d, red line) we obtain velocities between 0.237 and 0.276 m/ns, with an average uncertainty of 0.01 m/ns, corresponding to densities of 313 to 145 kg/m^3. It is unlikely that the snow density is as low as 145 kg/m^3, and the velocity measurements that yield such unlikely results are confined to the region between x ~30 -55 meters. Either the diffractors along this part of the line are all too large to meet our point diffractor assumption, or the noise levels in the image are higher than the signal.

Excluding the picks between x=30 and 55 meters, we estimate snow densities between 193 and 311 kg/m^3, with an average density of 274 kg/m^3. Notably, the low-density estimates are from the part of the profile near x = 55 to 65 meters where a prominent set of mid-snow diffractors exist. The two-way travel time to the tops of these diffractors is ~7.414 ns, which at the observed migration velocity of 0.256 m/ns yields a depth estimate of ~0.95 meters. Thus, this snow density estimate of 193 kg/m^3 corresponds to the upper 0.95 meters of snow. Estimated snow depths, densities and SWE along the entire profile are shown in Figure 7.

We measured snow density and depth in Pit 1 located at 68 meters along the Line 1 (Figure 7). The snow pit showed a depth of 1.33 meters and an average density of 300 +/- 40

Deleted: . We

Deleted: . Velocities on this line range from 0.23 to 0.25 m/ns with an average uncertainty of +/- 0.01 m/ns. Estimated snow-depths range from 1.6 to 1.9 meters with an average uncertainty of +/- 0.07 m. Estimated snow densities range from 0.23 to 0.36 g/cc with an average uncertainty of +/- 0.07 g/cc. Estimated SWE ranges from 0.3 to 0.5 meters with an average uncertainty of 0.08 meters (Figure 8). ... [10]

Deleted: a pit

Deleted: profile.

Formatted: Indent: First line: 0.5"

Deleted: 0.30 +/- 0.04 g/cc

kg/m^3 resulting in a SWE measurement of 0.40 +/- 0.07 meters. GPR derived estimates at the pit location are: snow depth = 1.28 +/-0.06 meters, density = 288 +/- 50 kg/m^3, SWE = 0.37 +/- 0.07 meters. The average density of the upper 0.95 meters of snow in this pit is 190 kg/m^3 (Fig S1), which is very close to the value estimated from the GPR data between x = 55 and x = 65 meters.

3.3 Snowmobile-Mounted GPR data

We collected four GPR profiles in the snowmobile-mounted configuration between Feb 25 and March 17, 2015. Here we discuss the processing of a representative profile, Line 4 (Figure 8), which was collected on the morning of March 11, 2015 in a flat meadow just south of Wyoming State Highway 130. This line is 98 meters long and shows an abundance of diffractions along the snow/ground interface (Figure 8). After interpolating to equal spacing, the trace spacing was 0.024 m.

Migration velocities on this line range from 0.237 to 0.277 m/ns with an average uncertainty of +/- 0.01 m/ns. The corresponding snow velocities are 0.207 and 0.268 m/ns. Here, the exceptionally high velocities are confined to a region between x = 65 and x= 85 meter where a number of diffractions from obviously large objects are present (Figure 7). If we exclude velocity picks from this region, we get a maximum migration velocity of 0.266 m/ns and a maximum snow velocity of 0.251 m/ns. Estimated snow depths range from 0.7 to 2.1 meters with an average uncertainty of +/- 0.1 m. Estimated snow densities range from 228 to 532 kg/m^3 with an average uncertainty of +/- 50 kg/m^3. Estimated SWE ranges from 0.25 to 0.71 meters with an average uncertainty of +/- 0.09 meters.

Deleted: 0.32 +/- 0.07 g/cc, SWE = 0.41 +/- 0.07

Deleted:

Deleted: Line 07

Deleted: 9a). Picking velocities along this line required significantly more discretion than was required on Line 19. Whereas on Line 19 we were confident in choosing velocities with well-defined varimax peaks, on this line we rejected some velocity observations between x = 0 and x = 10 that appeared to produce well focused diffractions that would have resulted in snow-density estimates greater than 1 g/cc.

Deleted: Velocities

Deleted: 22

Deleted: 24

Deleted: 012

Deleted: 6

Deleted: .8

Deleted: 07

Deleted: 0.27

Deleted: 0.45 g/cc

Deleted: 0.05 g/cc

Deleted: 26

Deleted: 8

Deleted: 08

Snowpits 3 and 4 are located at 50 and 97 meters along the profile and showed average snow densities of 379 +/- 50 and 360 +/- 48 kg/m^3; SWE values of 0.54 +/- 0.13and 0.64 +/- 0.13 meters; snowdepth was 1.44 +/- 0.05 and 1.8 +/- 0.05 m respectively. The GPR-derived depth, density and SWE estimates at 50 and 97 meters were 1.50 +/- 0.08 and 1.91 +/- 0.12 m; 389 +/- 92 and 394+/- 97 kg/m^3,; and 0.53 +/- 0.09 and 0.70 +/- 0.13 m. GPR-derived estimates for the whole profile are shown in Figure 9. We also measured 21 snow depths at 5 meter intervals (Figure 9b) along this profile. The RMS error between observed and estimated depths is 0.13 meters.

During data acquisition on Line 7, the air temperature was 5° C, raising the possibility of liquid water in the snow. The average frequency of the snow reflection for every trace in the image is 435 MHz with a standard deviation of 27 MHz and the average frequency of the soil reflection across the whole line is 464 MHz with a standard deviation of 38 MHz. Again, the frequency content of the soil reflection appears to be higher than the reference frequency. Within the uncertainty bounds there is no resolvable frequency change and we conclude that our dry snow assumption is valid.

4. Discussion

The primary purpose of this study is to develop an efficient processing flow for measuring GPR velocity and thus snow density SWE from common-offset data that requires a minimum amount of human interpretation. Common-offset GRP data are fast and easy to obtain, and velocity estimates can be made when diffractions are present. However, the common methods of visually inspecting migrated images or fitting curves to diffraction hyperbolas are time-consuming and subject to human error. The migration velocity analysis described in this paper provides an efficient means for extracting velocity information from large GPR data sets. Here we discuss the accuracy and efficiency of the method as well as the level of automation.

To validate the method, we compared estimated snow densities, depths, and SWE to observations made in four snow pits and to 86 probed snow depth measurements. The results are summarized in Table 2 and in Figure 9. If we exclude the two obvious outliers (Figure 10a), the RMS error for our depth predictions for the remaining 88 depth observations is 12% of the mean snowdepth observation. The RMS error for snow density and SWE relative to the mean observed values are 15% and 18%. Averaging the velocities across the entire line (Figure 10 red crosses) reduce the difference between predicted and observed depth values to an RMS error of 9%, suggesting that lateral variations in snow velocity are minimal. Averaging the velocities across the entire line reduces the RMS errors for density and SWE to 8% and 10%, respectively.

The greatest potential for systematic error in this analysis is the presence diffracting objects whose dimensions exceed the radius of the first Fresnel zone. The field data offer the opportunity to evaluate the influence of diffractor size on velocity estimates. Line 1, for example, shows four prominent diffractions between 50 and 70 meters. The Varimax norm has a maximum value at 0.256 m/ns, which is the velocity that focuses the two leftmost diffractions (Figure 6c). The diffractions on the right are clearly not focused because they are caused by an object (most likely a log) with a radius greater than the first Fresnel zone. Because the leftmost two have a higher amplitude then the others, they have the largest influence on the varimax value. Thus, although there are clearly events in the field data that have the potential to give

Deleted: can be

Deleted:

Deleted: performance

Deleted: this

Deleted: .

Deleted:

erroneous results, our results suggest that reliable velocity estimates can be achieved so long as the majority of the diffracted energy is related to objects that can be considered point diffractors.

One of our main goals was to produce a processing flow that allows for the rapid processing of common offset GPR data with minimal user interaction. The two most time computationally expensive parts of the processes are the migrations and the varimax calculations. As an example, on a 2016 MacBook Pro with a 2GHz processor, for the ~ 100-meter-long Line 4, performing 51 migrations takes approximately 5 minutes, the varimax calculation takes about half as long, and the PWD filtering takes a few seconds. The most time-consuming part of the process is picking the arrival times of snow surface and ground surface reflections.

Although the processing flow is relatively efficient, it does require some user interaction. The PWD method of separating continuous reflectors from diffractions treats the GPR image as the superposition of locally planar waves. Estimating the slope of these waves from the image requires the solution of a regularized inverse problem and the smoothness of the slope-field depends on the choice of regularization parameter. This is the most subjective step of the process, as it may require several attempts to find the optimal smoothness constraints to adequately suppress reflections in the GPR image. However, for our data the majority of the diffractions are located along the ground surface and the internal structure of the snowpack shows dips that closely parallel the ground reflection. A good first guess, and often a good final guess, for the dip field can be computed by picking the arrival times of the

Deleted: We found that areas of rapidly changing slope can result in noise from incompletely suppressed reflection events and poorly preserved diffractions. Noise from inadequate filtering may cause the Varimax Norm value to be high even when the diffractions are not optimally focused and low when they are. Visually checking the migrated images before committing to a velocity pick can help mitigate this issue.

ground reflection. Because the ground reflection has to be interpreted to measure snow depth, this strategy can significantly reduce the processing time for each data set.

The data presented in this paper contained an abundance of diffractions located near the soil/ground interface allowing an average velocity for the entire snowpack to be obtained. These events are likely due to small-scale variations in surface topography, rocks, and/or vegetation along the ground surface, which may not be present in all environments. However, we note that mountain watersheds free of vegetation, small undulations in surface topography, and surface rocks are probably rare. Thus, the method may be useful in many regions where seasonal snowpacks exist.

5. Conclusions

We applied the migration focusing analysis presented in Fomel (2007) to the problem of estimating SWE in seasonal snow. The method was most accurate for the case when the GPR was in contact with the snow, providing GPR-derived SWE estimates within 6 % of the manual observation. When the GPR was mounted on a snowmobile, the results were within 12-21% of the manual observations.

Deleted: In particular, Line 7 required a substantial amount of user intervention to avoid picking obviously incorrect velocities. The performance of the MVA analysis along this line may have been due to several complicating factors: 1. When mounted on the snow-mobile, the GPR antenna is fixed at the rear and can wobble up and down at the front by up to ~5 cm. The change in orientation of the antenna with respect to subsurface targets as well as the change in distance between the snow surface and the GPR antenna may be additional noise sources and cause diffractions to migrate incorrectly. This situation is likely to be of concern when the snow-surface is uneven, or when the snowmobile is accelerating. Indeed, the greatest variability along this line occurred during the first few meters when the snowmobile was accelerating. 2. On this day the air-temperatures were above freezing and, although our frequency analysis suggests that we can make the dry snow assumption, it is likely that some water was present in the snowpack the presence of water in the snowpack would result in decreased velocities and increase the apparent dry snow density. ... [11]

Deleted: the presence of

Deleted: small bushes near the base of the snow-pack

Deleted: Areas likely to contain point diffractors suitable for this type of analysis can

Deleted: scouted for ahead of time during the summer months or on aerial photographs.

Deleted: when

Deleted:

Deleted: were

Deleted: 3

Deleted: 18

Deleted: The processing flow that we presented in this paper proved to be an efficient way to measure radar velocities within seasonal snow. While not fully automated, the method requires less processing time than visually scanning each migrated image and could make GPR a more attractive tool for estimating SWE at the watershed ... [12]

Formatted: Font:Not Bold

Formatted: None

Acknowledgements

This work was funded by the U. S. National Science Foundation (NSF) EPSCoR Program, NSF award EPS-1208909. We would like to thank Matt Provart for assisting with data collection and Mehrez Elwaseif for assistance with REFLEX software. Data used in this paper are available at https://data.uwyo.edu.

Deleted: Wyoming

Deleted: also

References and notes

Bales, R. C., Motlotch N. P., Painter, T. H., Dettinger, M. D., Rice, R., and Dozier, J.: Mountain hydrology of the western United States, *Water Resour. Res.,* 42, 2006.

Bradford, J. H.: Frequency dependent attenuation analysis of ground-penetrating radar data, *Geophysics*, 72, 2007.

Bradford, J. H. and Harper, J. T.: Wave-field migration as a tool for estimating spatially continuous radar velocity and water content in glaciers, *Geophys. Res. Let.,* 32, 2005.

Bradford, J. H., Harper J. T., and Brown, J.: Complex dielectric permittivity measurements from ground-penetrating radar data to estimate snow liquid content in the pendular regime, *Water Resour. Res.,* 45, 2009.

Claerbout, J. F.: Imaging the Earth's interior: Blackwell Scientific Publications, Inc. 1985.

Claerbout, J. F.: Earth soundings analysis: Processing versus inversion: Blackwell Scientific Publications, Inc. 1992.

Conger, S. M. and McClung, D. M.: Instruments and methods comparison of density cutters for snow profile observations, *Journal of Glaciology*, 55, 163-169, 2009.

Dix, C. H.: Seismic velocities from surface measurements, *Geophysics*, 20, 68-86, 1955

Fomel, S.: Local seismic attributes, *Geophysics,* 72 (3), 2007.

Fomel, S., Landa, E., Taner M. T.: Poststack velocity analysis by separation and imaging of seismic diffractions, *Geophysics,* 72, 89-94, 2007.

Fomel, S.: Applications of plane-wave destruction filters, *Geophysics,* 67(6), 1,946-1,960, 2002.

Holbrook, W. S., Miller, S. N., and Provart, M. A.: Estimating snow water equivalent over long mountain transects using snowmobile-mounted ground-penetrating radar, *Geophysics,* 81, 2016.

Landa, E. and S. Keydar.: Seismic monitoring of diffraction images for detection of local heterogeneities, *Geophysics*, 63, 1998.

Molotch, N., and Bales, R. C.: Scaling snow observationf from the point to the grid element: Implications for observation network design, *Water Resour. Res.*, 41, 2005.

Formatted: refs, Indent: Left: 0", First line: 0", Line spacing: single

Nash, J. E. and Sutcliffe, J. V.: River flow forecasting through conceptual models part I – A discussion of principles, *J. Hydrology,* 10, 282-290, 1970.

Serreze, M. C., Clark, M. P., Armstrong, R. L., McGinnis, D. A., and Pulwarty, R. S.: Characteristics of the western United States snowpack from snowpack telemetry (SNOTEL) data, *Water Resour. Res.*, 35, 2,145-2,160, 1999.

Sheriff, R. E.: Nomogram for Fresnel-zone calculation, *Geophysics,* 45, 1980.

Stolt, R. H.: Migration by Fourier Transform, *Geophysics*, 43, 23-48, 1978.

Formatted: refs, Indent: Left: 0", First line: 0", Line spacing: single

Tiuri, M. E., Sihvola, A. H., Nyfors, E. G., and Hallikaiken, M. T.: The complex dielectric constant of snow at microwave frequencies, *IEEE J. Oceanic Eng. OE-9*(5), 377-382, 1984.

Turner, G., and A. F. Siggins.: Constant Q attenuation of subsurface radar pulses, *Geophysics*, 59, 1994.

Tzanis, A.: MATGPR: A freeware MATLAB package for the analysis of common-offset GPR data, *Geophysical Research Abstracts*, 8, 2006.

Formatted: refs, Indent: Left: 0", First line: 0", Line spacing: single

Wiggins, R. A.: Minimum entropy deconvolution, *Geoexploration* (16), 21-35, 1978

Figure Captions

Figure 1 a) Synthetic hyperbolas for 4 rectangular diffractors with lateral dimensions of 0.1, 0.2, 0.3 and 0.4 meters (from left to right) and a round diffractor with radius = 0.4 meters (far right.) **b)** Varimax curve for windows depicted in **a**, V curve colors match the windows in **a.** V curves for all four rectangular diffractors show peaks at 0.24 m/ns, while the round diffractor is peaked at 0.268 m/ns. **c)** Varimax curve for the entire image showing a peak at the correct migration velocity of v = 0.24 m/ns.

Figure 2 Justification for uncertainty estimates. A synthetic hyperbola that is obviously undermigrated (**a**), migrated at indistinguishable velocities (**b-d**), and obviously overmigrated (**e**). **f)** The corresponding varimax curve for **a-e** showing a peak at the true migration velocity (0.24 m/ns), the shaded area under the curve corresponds to velocities in **b-d** and represent varimax values that are 95% of the maximum. Panels (**g-l**) show the same for a section of field data extracted from Line 1.

Figure 3 Raypaths and travel-times for point diffractors. **a)** 0.5 meters of air overlying a 230 m/ns snowpack with point diffractors buried at 0.5 meter intervals. **b)** two-way travel-times for each of the diffractors showing the characteristic hyperbolic shape.

Figure 4 Dix velocities for point diffractors as a function of depth for different hyperbola widths. The true interval velocity is 0.230 m/ns (red line) and the Dix velocities are shown as

Formatted: Font:Bold

Deleted: **Figure 1**

Deleted: 2

black lines. The red dashed line is at 0.234 m/ns, which is 2 percent greater than the true velocity.

Figure 5 Synthetic Data set and velocity picking. **a)** synthetic data before filtering. **b)** after PWD filtering. **c)** Varimax norm for sliding window 8 meters wide **d)** Velocities from synthetic data set as a function of diffractor depth. Solid blue line shows measured migration velocities, dashed blue lines show uncertainty bounds. Solid red line show velocities computed with the Dix equation, dashed red lines show uncertainty bounds. Solid black line shows the true velocity (0.24 m/ns). Light gray region indicates where velocities are within 2% of the true velocity and dark gray region shows where velocities are with 5% of the true velocity.

Figure 6 **a)** raw GPR data for Line 1 **b)** GPR data after PWD filtering **c)** diffractions migrated at the mean velocity (0.245 m/ns) for the entire line **d)** Normalized varimax curves for sliding window 10 meters wide. Blue curve shows the peak value for every curve, red line is smoothed with a box car averaging filter 10 meters wide.

Figure 7 Line 1 Results. **a)** density, **b)** snow depth (black line) and SWE (blue line) estimates from the GPR data, snow pit data are shown in red. Grayed out region corresponds to areas where velocity picks are unreliable.

Figure 8 **a)** raw GPR data for Line 4, red lines indicate interpreted ground and snow reflection. **b)** GPR data after PWD filtering **c)** diffractions migrated at the mean velocity (0.256 m/ns) for

Deleted: **Figure 3** Snow wetness for typical GPR velocities in and snow and peak frequency shifts for a reference frequency of 500 MHz. For the data presented in this paper, typical uncertainties in the frequency measurements are 10 to 40 MHz and the velocities range from 0.22 m/ns to 0.25 m/ns. For the typical range of velocity and frequency shift estimates reported in this paper, snow wetness values less than 0.03 cannot be resolved. ... [13]

Deleted: **b)** the unmigrated data

Deleted: , black box indicates windowed portion of the data used to calculate the Varimax norm.

Deleted: plotted against velocity showing a peak at 0.246 m/ns.

Deleted: windowed portion of the data migrated at 0.246 m/ns showing focused diffraction events. ... [14]

Formatted: Font:Bold

Deleted: Synthetic data set from a model with the lateral velocity trend and no air layer. **b)** The recovered velocities (black line) show the same trend as the true model (red) but systematically underestimate the true values by 2.1% at x = 0 meters and 1.6 % at x = 10 meters. ... [15]

Deleted: .

Deleted: unmigrated

Deleted: , black box indicates windowed portion of the image used to compute the varimax norm

Deleted: Varimax norm for windowed data as a function of migration velocity showing a peak at 0.250 m/ns **d)** windowed portion of the data

Deleted: 0.250 m/ns showing the focused diffraction events.

Formatted: Font:Not Bold

Deleted: **8**

Deleted: 19

Deleted: **a)** the radar velocity within the snow along the profile.

Deleted: **c)** snow densities estimated from the GPR data (blue line) and the density measured in the snow-pit at 68 meters (red).

Deleted: **9** Velocity Picking Line 07.

Deleted: unmigrated

Deleted: .

Deleted: unmigrated

Deleted: , black box indicates windowed portion of the image used to compute the varimax norm

Deleted: Varimax norm of the windowed data as a function of velocity showing a peak of 0.254 m/ns **d)** windowed portion of the data

Deleted: 0.254 m/ns showing the focused diffraction events. ... [16]

the entire line **d)** Normalized varimax curves for sliding window 10 meters wide. Blue curve shows the peak value for every curve, red line is smoothed with a box car averaging filter 10 meters wide.

Figure 9 Line 1 Results. **a)** density, **b)** snow depth (black line) and SWE (blue line) estimates from the GPR data, snow pit data are shown in red. Grayed out region corresponds to areas where velocity picks are unreliable.

Figure 10 Cross-plots of predicted data (horizontal axis) vs GPR estimates (vertical axis) for all data. **a)** snowdepths, **b)** density, and **c)** SWE. Black crosses represent estimates using automatically picked velocities and red crosses represent estimates using the mean velocity for each GPR profile.

Deleted: Line 07 results. **a)** radar velocity along the profile.

Formatted: Font:Not Bold

Deleted: as well as the probe depths (red) and the

Deleted: at 50 and 97 meters (red). **c)** snow densities estimated from the GPR data (blue line) and the densities measured

Deleted: pits at 50 and 97 meters (

Deleted:).

Deleted: **11**

Deleted: plot

Deleted: snow depths measured with snow-probe (x-axis) and snow-depths

Deleted: from GPR

Deleted: y-

Deleted:). R^2 = 0.95.

Section Break (Next Page)

.Figures

Figure 1

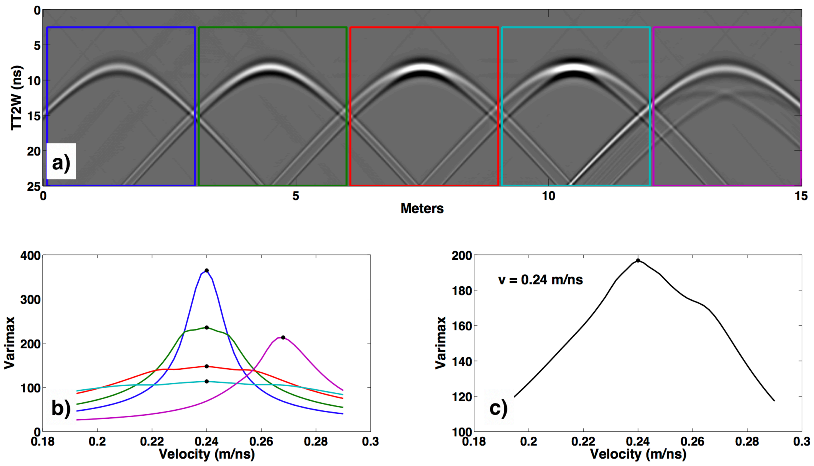

Formatted: None

Deleted: ... [17]

Formatted: Font:Bold

Formatted: Font:Bold

Figure 2

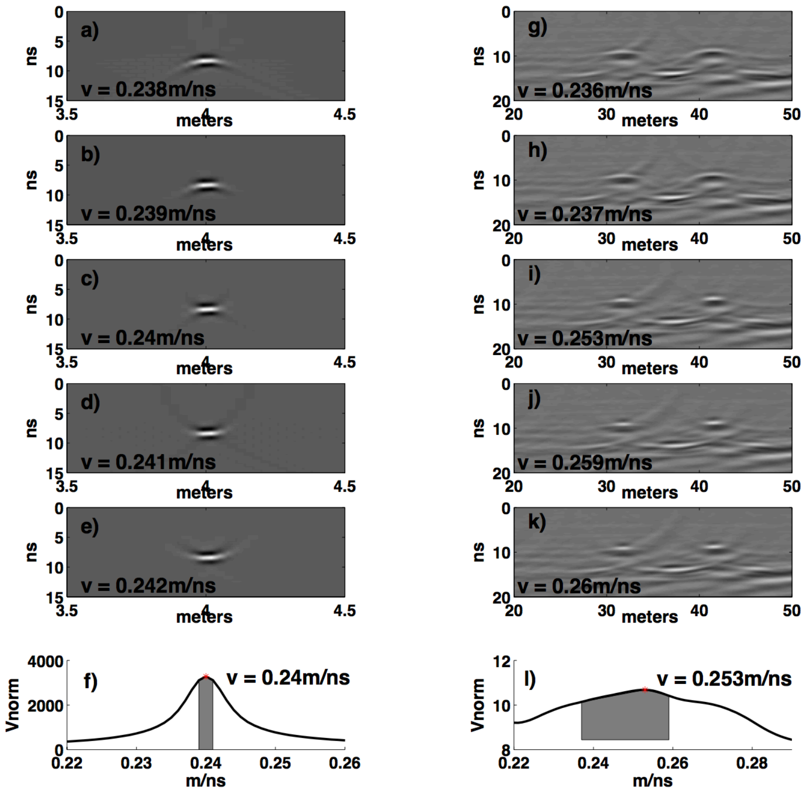

Formatted: None

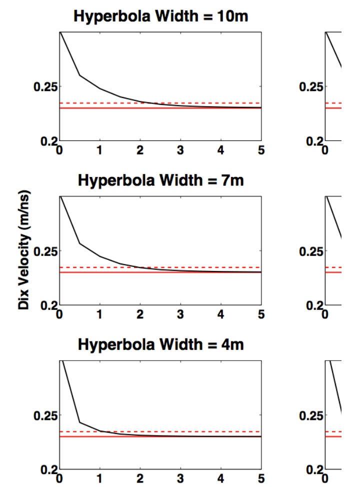

Deleted: ... [18]

Formatted: Font:Bold

Formatted: Level 1

Figure 3

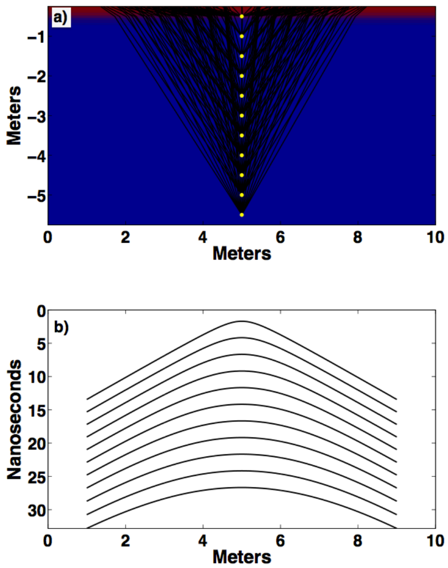

Formatted: Font:Not Bold

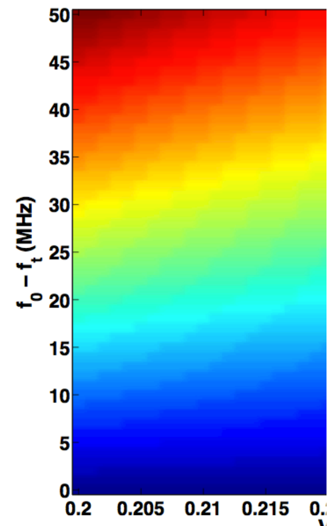

Deleted: ... [19]

Formatted: Font:Bold

Formatted: Font:Bold

Formatted: Font:Not Bold

Figure 4

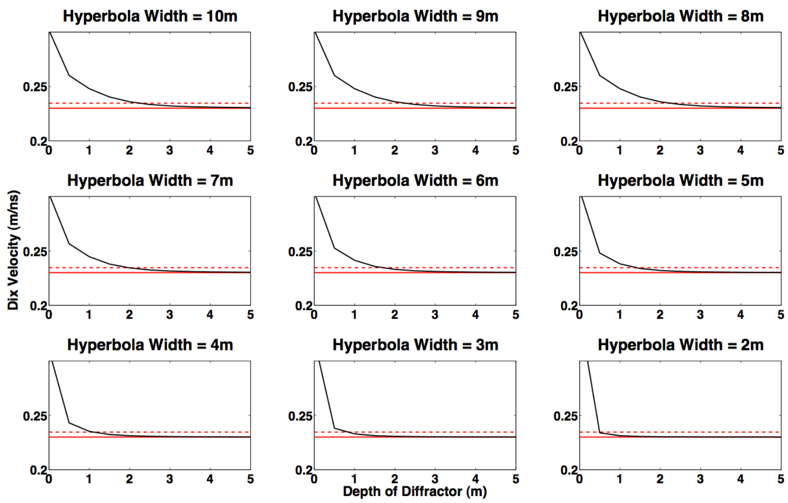

Formatted: Level 1

Deleted: ... [20]

Formatted: Font:Bold

Figure 5

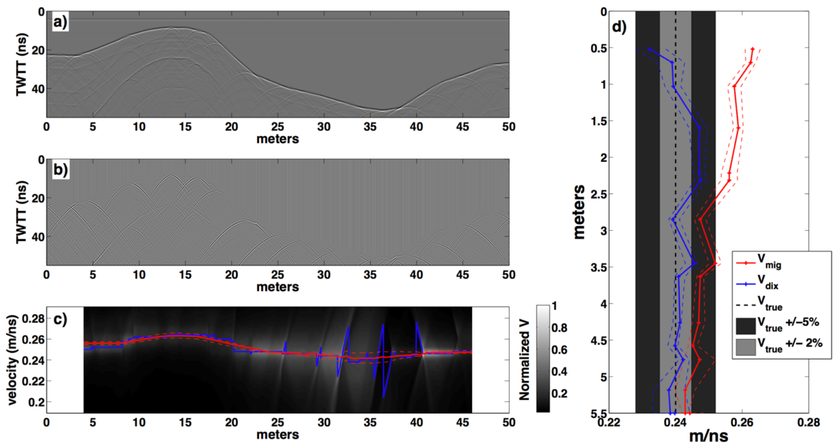

Figure 6

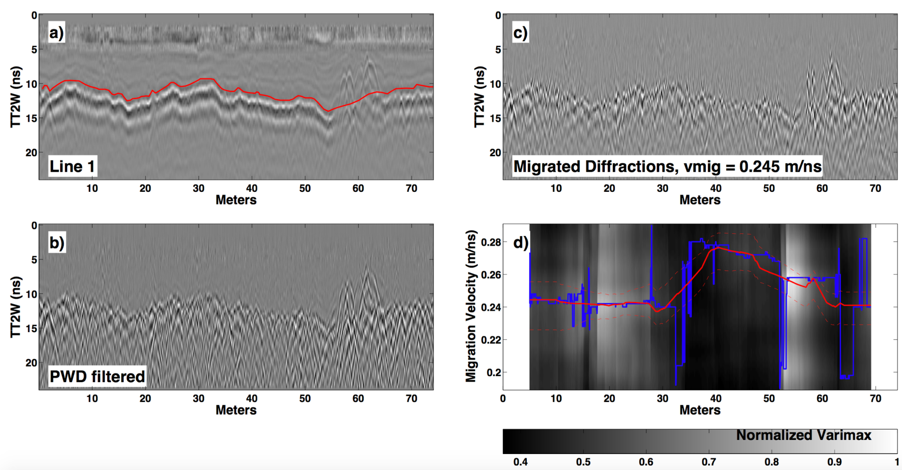

Formatted: None

Formatted: Font:Bold

Deleted: ... [21]

Formatted: Font:Bold

Formatted: Font:Bold

Formatted: Font:Bold

Figure 7

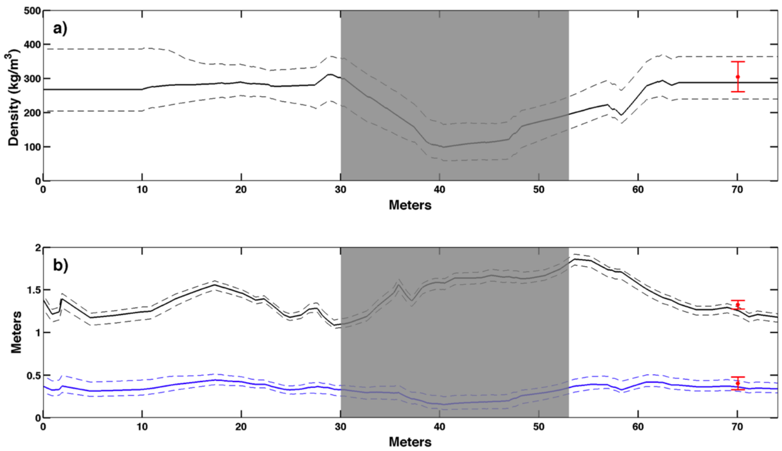

Figure 8

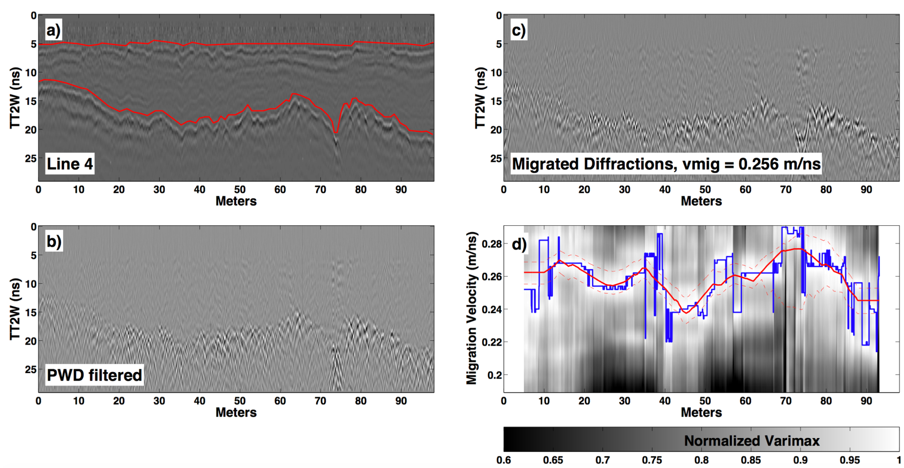

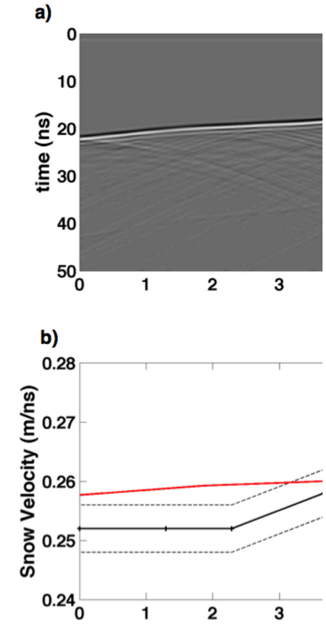

Deleted: ... [22]

Formatted: Font:Bold

Formatted: None

Formatted: Font:Bold

Formatted: Font:Bold

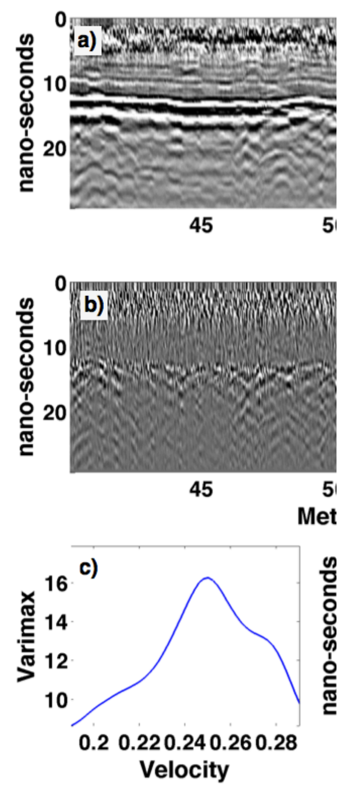

Deleted: ... [23]

Formatted: Font:Bold

Formatted: None

Formatted: Font:Bold

Figure 9

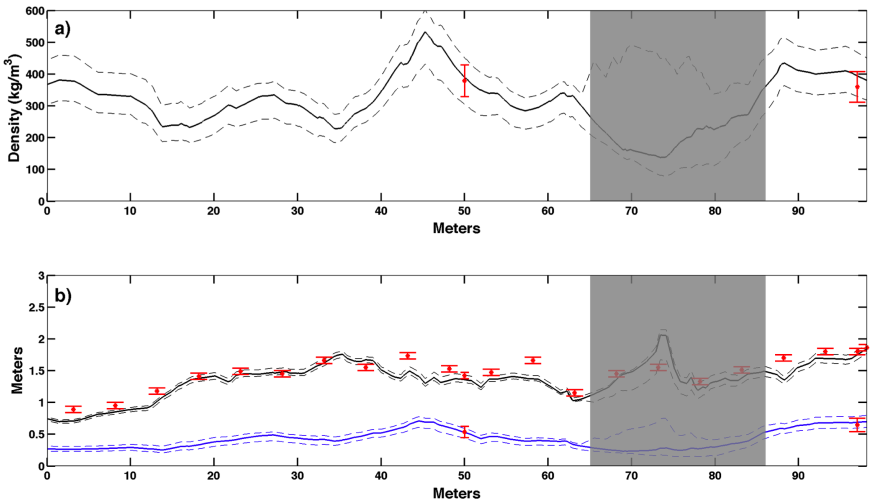

Deleted:

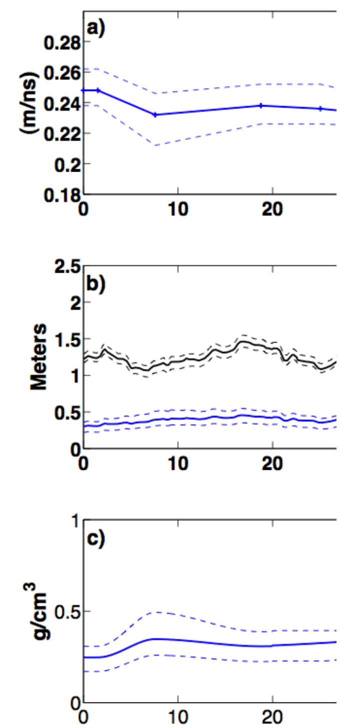

... [24]

Formatted: None

Formatted: Font:Bold

Deleted: ... [25]

Formatted: Font:Bold

Figure 10

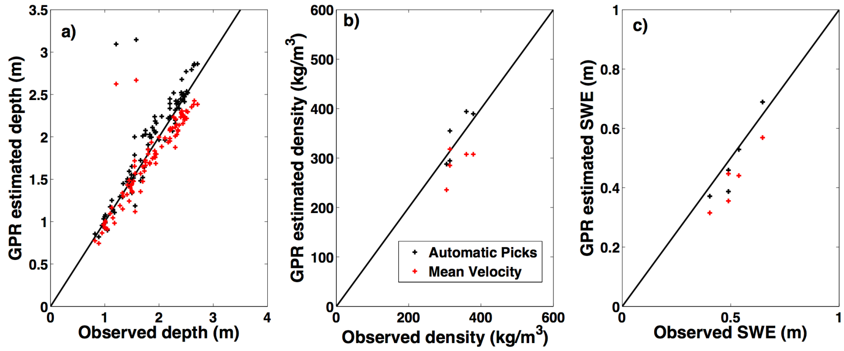

Formatted: None

Deleted: ... [26]

Formatted: Font:Bold

Formatted: Font:Bold

Tables

Table 1. Snowpit summary

Pit Name	Date	Depth (m)	Rho (kg/m^3)	SWE (m)	GPR profiles
Pit 1	25-Feb-15	1.33 +/- 0.05	305 +/- 44	0.40 +/- 0.14	Line 1
Pit 2	26-Feb-15	1.56 +/- 0.05	314 +/- 44	0.49 +/- 0.14	Lines 2 and 3
Pit 3	11-Mar-15	1.44 +/- 0.05	379 +/- 50	0.55 +/- 0.13	Line 4
Pit 4	11-Mar-15	1.80 +/- 0.05	360 +/-48	0.65 +/- 0.13	Line 4

Table 2. Summary of GPR field data and comparison to manual measurements

				GPR Predictions at pit			Error Compared to Pit/Probe		
GPR Profile	**Collection Date**	**Acquisiton Mode**	**Pits/Probe**	**Depth Pred (m)**	**Rho (kg/m^3)**	**SWE (m)**	**Depth**	**Rho**	**SWE**
Line 1	25-Feb-15	Ski	Pit 1	1.29 +/-0.06	288 +/- 50	0.37 +/- 0.07	2.6%	5.5%	8.0%
†Line 2	25-Feb-15	Ski	Pit 2	1.59 +/- 0.04	294+/-40	0.46+/- 0.03	0.1%	6.0%	6.0%
†Line 3	25-Feb-15	Snowmobile	Pit 2	1.10 +/- 0.05	354 +/-65	0.39 +/ 0.06	*30.0%	13%	*21%
Line 4	11-Mar-15	Snowmobile	Pit 3 Pit 4 Probes	1.50 +/- 0.08 1.91 +/- 0.12	389 +/-92 394 +/- 97	0.53+/- 0.09 0.69 +/- 0.13	6.0% 6.0% **RMSE = 0.13 m (9%)	3% 10%	2.0% 6.%
†Line 5	17-Mar-15	Snowmobile	Probes				**RMSE = 0.38 m (18%)		
†Line 6	17-Mar-15	Snowmobile	Probes				**RMSE = 0.19 m (11%)		

*Line 3 was located 1.5 meters off of Pit 2, disagreement between depth and SWE measurements at this site reflect lateral variations in snowdepth.

**RMSE percentages are calculated relative to the mean observed depth along each profile

†Lines 2, 3, 5, and 6 are described in the supplementary materials.

Supplementary Materials

In addition to the data presented in the main text, we include snow density profiles for Pits 1-4 (Figure S1) and show data and results for GPR lines 2, 3, 5 and 6:

Line 2 is a skier pulled data set collected on February 25, 2015 in sub-freezing conditions. Pit 2 was located at x = 100 meters. After interpolating the data to equal spacing, the trace spacing was 0.027 meters. The data and velocity picks are depicted in Fig S2 and the resulting snow depth, density and SWE estimates are shown in Fig S3.

Line 3 is a snowmobile driven data set collected on February 25, 2015 in sub-freezing conditions. Pit 2 was located at x = 54 meters. After interpolating the data to equal spacing, the trace spacing was 0.027 meters. The data and velocity picks are depicted in Fig S4 and the resulting snow depth, density and SWE estimates are shown in Fig S5. Notably, Pit 2 was located ~1.5 meters off of the GPR line, which we suggest explains the discrepancy in the depth and SWE predictions at the pit site.

Line 5 is a snowmobile driven data set collected on March 17, 2015 in above-freezing conditions. Air temperature reached 10° C on this day and we infer that the dry snow assumption was not valid. After interpolating the data to equal spacing, the trace spacing was 0.0245 meters. The data and velocity picks are depicted in Fig S6 and the resulting snow depth, density and SWE estimates are shown in Fig S7. We probed snowdepth along this line at 2 meter intervals.

Line 5 is a snowmobile driven data set collected on March 17, 2015 in above-freezing conditions. Air temperature reached 10° C on this day and we infer that the dry snow assumption was not valid. After interpolating the data to equal spacing, the trace spacing was 0.0148 meters. The data and velocity picks are depicted in Fig S8 and the resulting snow depth, density and SWE estimates are shown in Fig S9. We probed snowdepth along this line at 2 meter intervals.

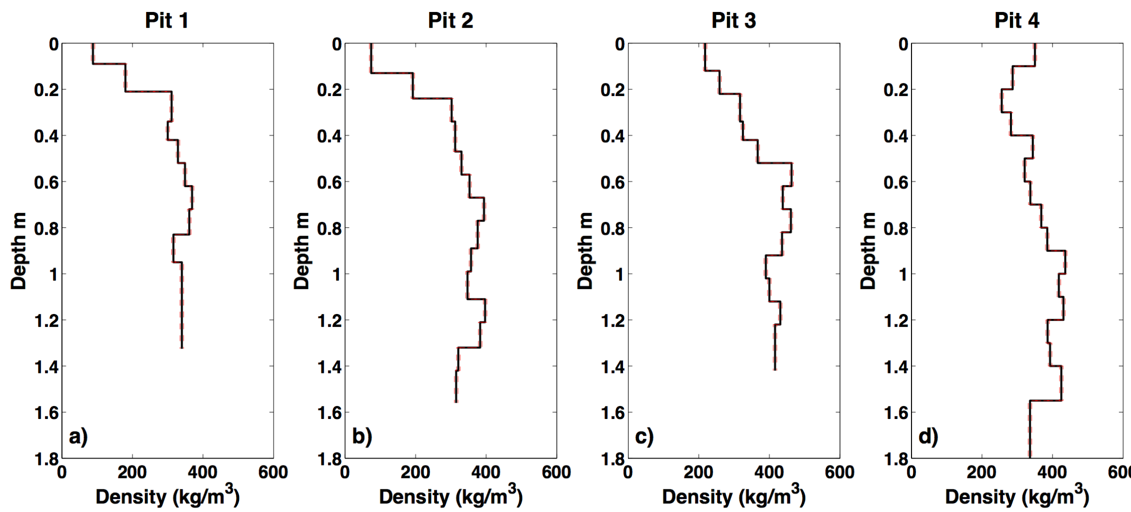

Figure S1. Snow density profiles. Black lines are measured density values, red lines indicate uncertainty estimate.

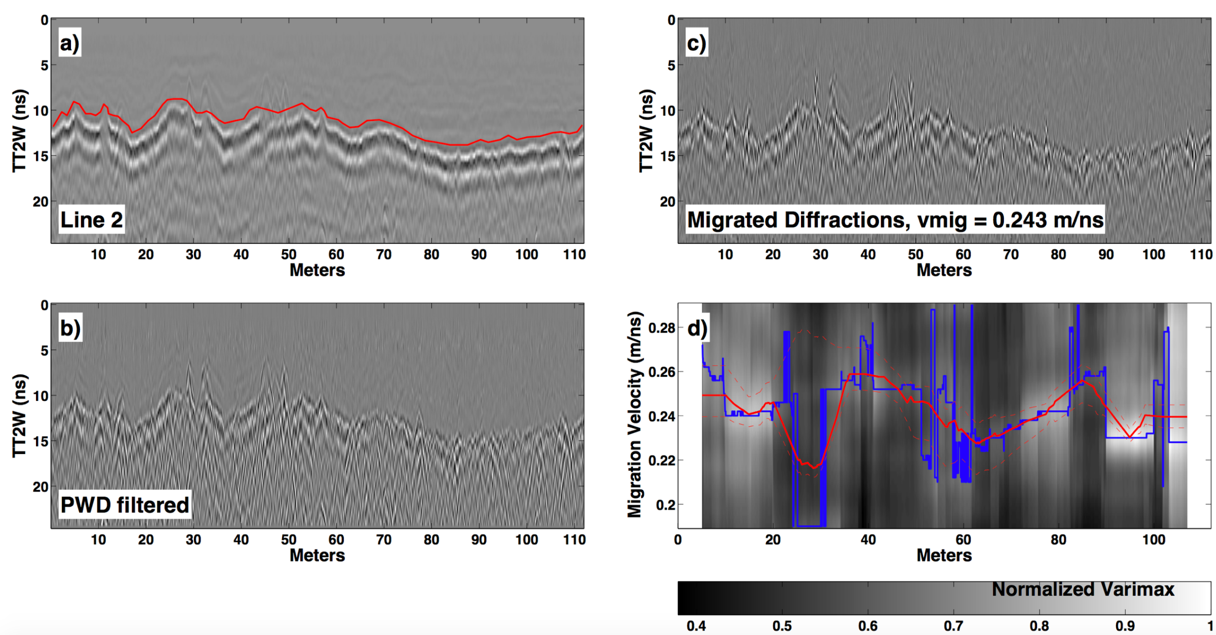

Figure S2. a) raw GPR data for Line, red line indicates interpreted ground reflection 2 **b)** GPR data after PWD filtering **c)** diffractions migrated at the mean velocity (0.243 m/ns) for the entire line **d)** Normalized varimax curves for sliding window 10 meters wide. Blue curve shows the peak value for every curve, red line is smoothed with a box car averaging filter 10 meters wide.

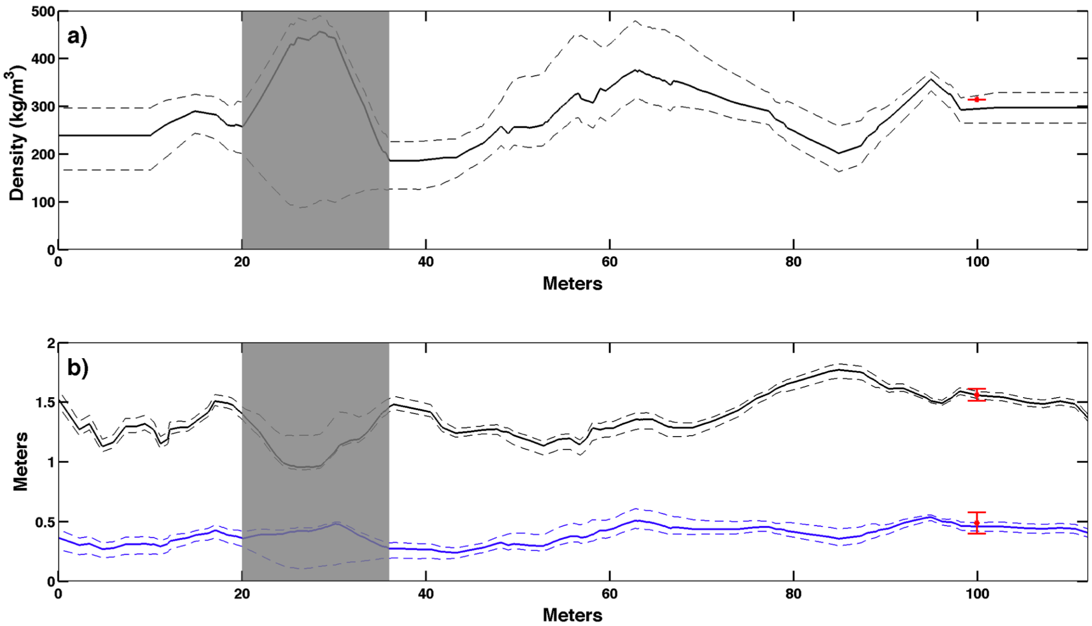

Figure S3. Line 2 Results. **a)** density, **b)** snow depth (black line) and SWE (blue line) estimates from the GPR data, snow pit data are shown in red. Grayed out region corresponds to areas where velocity picks are unreliable.

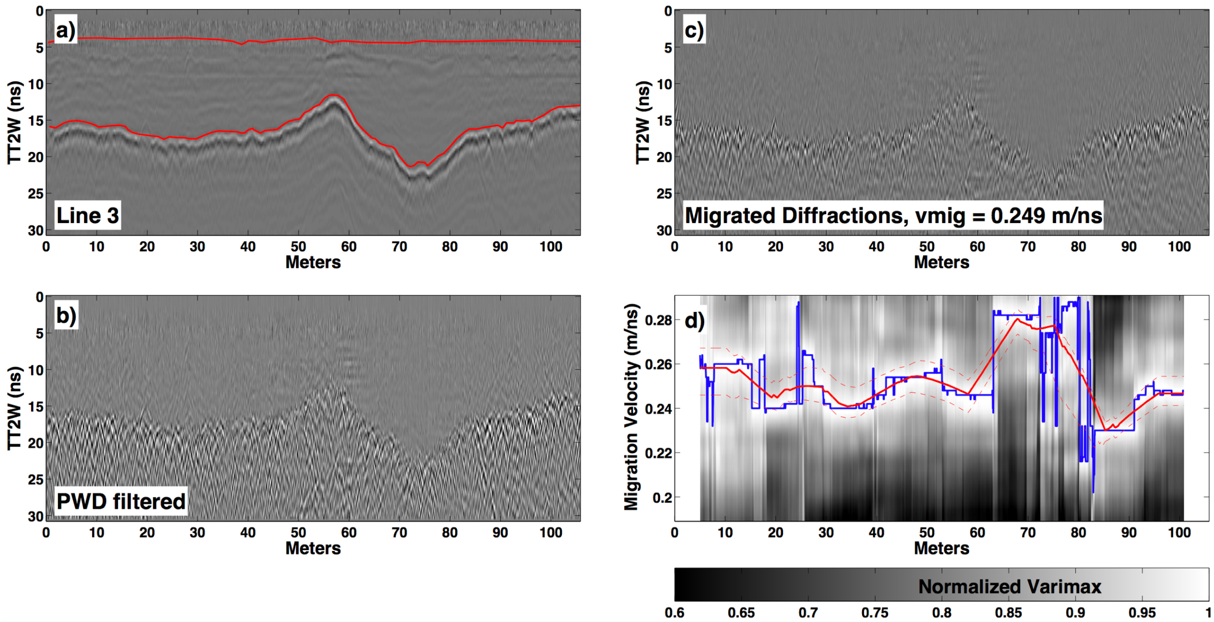

Figure S4. **a)** raw GPR data for Line 3, red lines indicates interpreted ground and snow reflections **b)** GPR data after PWD filtering **c)** diffractions migrated at the mean velocity (0.247 m/ns) for the entire line **d)** Normalized varimax curves for sliding window 10 meters wide. Blue curve shows the peak value for every curve, red line is smoothed with a box car averaging filter 10 meters wide.

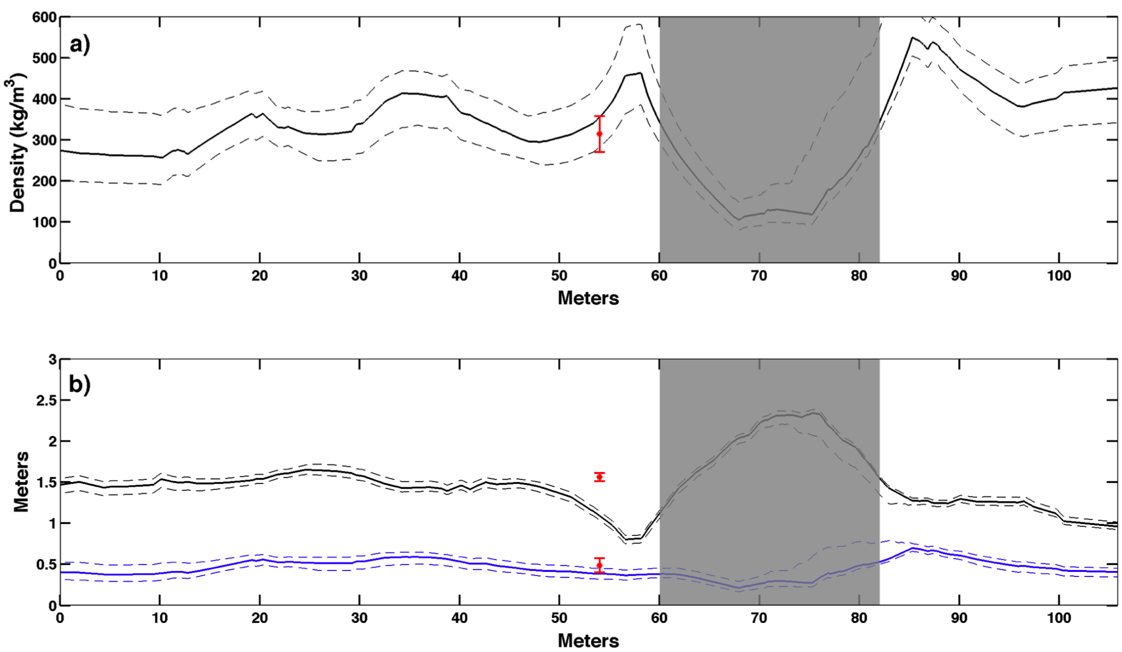

Figure S5. Line 3 Results. **a)** density, **b)** snow depth (black line) and SWE (blue line) estimates from the GPR data, snow pit data are shown in red. Grayed out region corresponds to areas where velocity picks are unreliable.

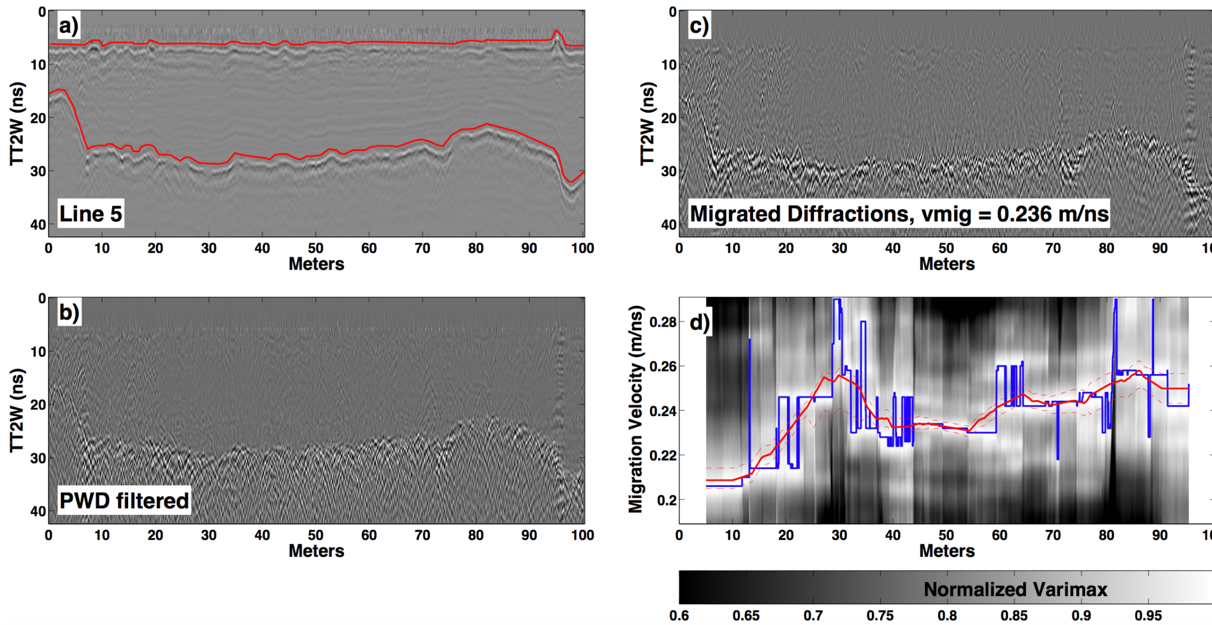

Figure S6. a) raw GPR data for Line 5, red lines indicates interpreted ground and snow reflections **b)** GPR data after PWD filtering **c)** diffractions migrated at the mean velocity (0.233 m/ns) for the entire line **d)** Normalized varimax curves for sliding window 10 meters wide. Blue curve shows the peak value for every curve, red line is smoothed with a box car averaging filter 10 meters wide.

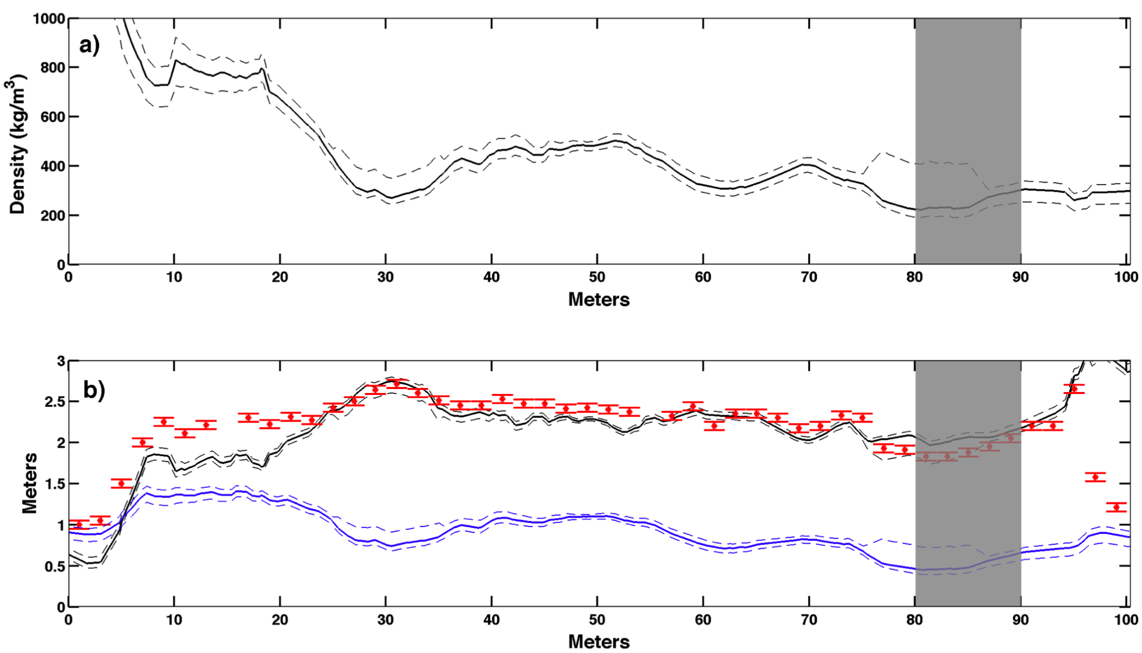

Figure S7. Line 5 Results. **a)** density, **b)** snow depth (black line) and SWE (blue line) estimates from the GPR data, snow pit data are shown in red. Grayed out region corresponds to areas where velocity picks are unreliable.

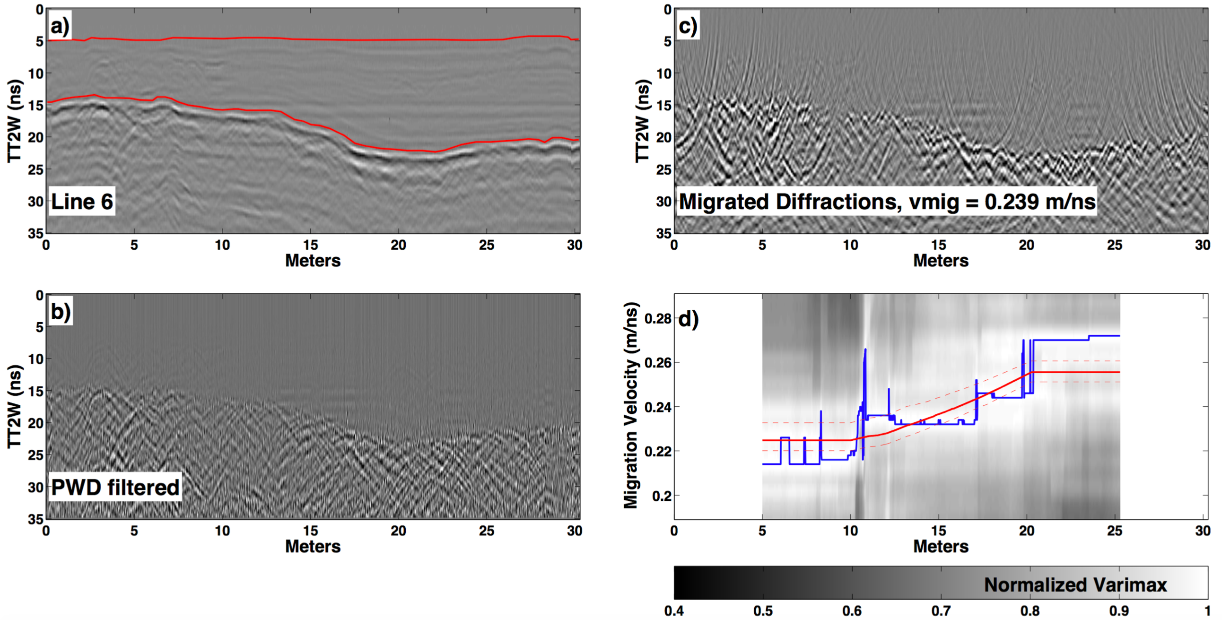

Figure S8. a) raw GPR data for Line 6, red lines indicates interpreted ground and snow reflections **b)** GPR data after PWD filtering **c)** diffractions migrated at the mean velocity (0.245 m/ns) for the entire line **d)** Normalized varimax curves for sliding window 10 meters wide. Blue curve shows the peak value for every curve, red line is smoothed with a box car averaging filter 10 meters wide.

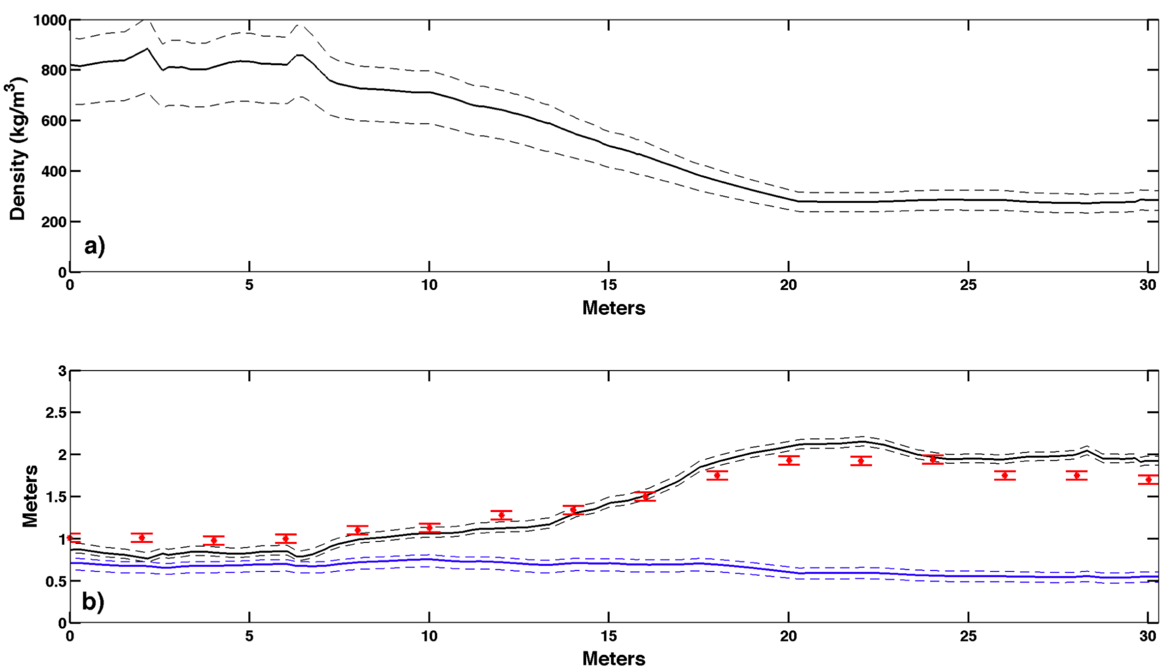

Figure S9. Line 6 Results. **a)** density, **b)** snow depth (black line) and SWE (blue line) estimates from the GPR data, snow pit data are shown in red.